https://doi.org/10.5194/acp-2021-13
Preprint. Discussion started: 22 March 2021

Atmospheric Chemistry and Physics Discussions

Reduction in C_2H_6 from 2015 to 2020 over Hefei, eastern China points to air quality improvement in China

Youwen Sun[1], Hao Yin[1,3,*], Cheng Liu[1,2,4,5,*], Emmanuel Mahieu[6], Justus Notholt[7], Yao Té[8], Xiao Lu[9], Mathias Palm[7], Wei Wang[1], Changong Shan[1], Qihou Hu[1], Min Qin[1], Yuan Tian[10], and Bo Zheng[11]

[1]*Key Laboratory of Environmental Optics and Technology, Anhui Institute of Optics and Fine Mechanics, HFIPS, Chinese Academy of Sciences, Hefei 230031, China*
[2]*Center for Excellence in Regional Atmospheric Environment, Institute of Urban Environment, Chinese Academy of Sciences, Xiamen, 361021, China*
[3]*University of Science and Technology of China, Hefei, 230026, China*
[4]*Key Laboratory of Precision Scientific Instrumentation of Anhui Higher Education Institutes, University of Science and Technology of China, Hefei, 230026, China*
[5]*Anhui Province Key Laboratory of Polar Environment and Global Change, USTC, Hefei, 230026, China*
[6]*Institute of Astrophysics and Geophysics, University of Liège, Belgium*
[7]*University of Bremen, Institute of Environmental Physics, P. O. Box 330440, 28334 Bremen, Germany*
[8]*Laboratoire d'Etudes du Rayonnement et de la Matière en Astrophysique et Atmosphères (LERMA-IPSL), Sorbonne Université, CNRS, Observatoire de Paris, PSL Université, 75005 Paris, France*
[9]*School of Engineering and Applied Sciences, Harvard University, Cambridge, MA 02138, USA*
[10]*Anhui University Institutes of Physical Science and Information Technology, Hefei 230601, China*
[11]*Institute of Environment and Ecology, Tsinghua Shenzhen International Graduate School, Tsinghua University, Shenzhen 518055, China*
*Corresponding authors.
E-mail addresses: chliu81@ustc.edu.cn (C. Liu), yhyh95@mail.ustc.edu.cn (H. Yin)

Abstract

Ethane (C_2H_6) is an important greenhouse (GHG) gas and plays a significant role in tropospheric chemistry and climate change. This study first presents and quantifies the variability, source, and transport of C_2H_6 over densely populated and industrialized eastern China by using ground-based high-resolution Fourier transform infrared (FTIR) remote sensing technique. We obtained a retrieval error of 6.21 ± 1.2 (1σ)% and degrees of freedom (DOFS) of 1.47 ± 0.2 (1σ) in retrieval of C_2H_6 tropospheric column-averaged dry-air mole fraction (troDMF) over Hefei, eastern China (117°E, 32°N, 30 m a.s.l.). The observed C_2H_6 troDMF reached a minimum monthly mean value of (0.36 ± 0.26) ppbv in July and a maximum monthly mean value of (1.76 ± 0.35) ppbv in December, and showed a negative change rate of (− 2.60 ± 1.34) %/yr from 2015 to 2020. The dependencies of C_2H_6 troDMF on meteorological and emission factors were analyzed by using generalized additive models (GAMs). Generally, both meteorological and emission factors have positive influences on C_2H_6 troDMF in cold season (DJF/MAM) and negative influences on C_2H_6 troDMF in warm season (JJA/SON). GEOS-Chem chemical model simulation captured the

https://doi.org/10.5194/acp-2021-13
Preprint. Discussion started: 22 March 2021

Atmospheric Chemistry and Physics Discussions

observed C_2H_6 troDMF variability and was thus used for source attribution. GEOS-Chem model sensitivity simulations concluded that the anthropogenic emissions (fossil fuel plus biofuel emissions) and the natural emissions (biomass burning plus biogenic emissions) accounted for 49.2% and 37.1% of C_2H_6 troDMF abundance over Hefei, respectively. The observed C_2H_6 troDMF abundance mainly results from the emissions within China (74.1%), where central, eastern, and northern China dominated the contribution (57.6%). Seasonal variability in C_2H_6 transport inflow and outflow over the observation site is largely related to the mid-latitude westerlies and Asian monsoon system. Reduction in C_2H_6 abundance from 2015 to 2020 mainly results from the decrease in local and transported C_2H_6 emissions, which points to air quality improvement in China in recent years.

Keywords: Remote sensing; FTIR; Ethane; Climate change; GAMs

1. Introduction

Ethane (C_2H_6) is an important greenhouse (GHG) gas and one of the most abundant Volatile Organic Compounds (VOCs) in the atmosphere (Abad et al. 2011; Singh et al. 2001; Steinfeld 1998). Although C_2H_6 is much less abundant than methane (CH_4) and also less efficient relative to mass, it plays a significant role in tropospheric chemistry and climate change (Tzompa-Sosa et al. 2017). In the presence of nitrogen oxides (NO_x = NO + NO_2), the C_2H_6 oxidation can enhance tropospheric ozone (O_3) generation, which shows a positive radiative influence on climate (Sun et al. 2018a) and threatens crop yields (Sun et al. 2018a; Van Dingenen et al. 2009) and human health (Sun et al. 2018a; Tzompa-Sosa et al. 2017). In addition, as a major source of acetaldehyde (CH_3CHO), C_2H_6 has a great impact on the production of peroxyacetyl nitrate (PAN) which is a key reservoir species of NO_x (Fischer et al. 2014). The main sink of tropospheric C_2H_6 is predominantly destruction via reaction with the hydroxyl radical (OH)(Xiao et al. 2008), which determines the residence time of most tropospheric species (Steinfeld 1998). As a result, tropospheric C_2H_6 can decrease the atmospheric oxidative capacity and indirectly impact the climate by extending the CH_4 lifetime (Monks et al. 2018; Taylor et al. 2020). Atmospheric C_2H_6 has a relatively long residence time of a few months (Franco et al. 2016), allowing it to undergo intercontinental transport. As a result, observations of C_2H_6 can be assimilated into a chemical transport model to estimate nonlocal emissions and air quality, and provide valuable insights into model biases of C_2H_6 simulations (Tzompa-Sosa et al. 2017).

On a global scale, the main sources of C_2H_6 are leakage from production, processing, and transport of natural gas (62%), biofuel combustion (20%) and biomass burning emission (18%), largely occurred in the Northern Hemisphere (NH) (Franco et al. 2016; Xiao et al. 2008). Additional minor sources of C_2H_6 are from biogenic and oceanic sources. However, on a regional scale, the proportion of each C_2H_6 source may show large difference. Natural gas leakage contribution can reach 80% of C_2H_6 emissions in regions with active oil and natural gas production (Gilman et al. 2013), where C_2H_6 emissions are highly correlated with CH_4 emissions. In such regions, C_2H_6 can be applied as a tracer for separation of fossil fuel CH_4 emissions from multiple methane (CH_4) sources (e.g., oil and gas, cows, wetlands, and rice yield) (McKain et al. 2015; Roscioli et al. 2015). The C_2H_6 abundance in the Southern Hemisphere (SH) is much lower than those in the NH since the anthropogenic C_2H_6 sources are low in the SH, and the residence time of C_2H_6 is shorter than the interhemispheric exchange rate. Many studies concluded that C_2H_6 in the SH is primarily emitted

https://doi.org/10.5194/acp-2021-13
Preprint. Discussion started: 22 March 2021

Atmospheric Chemistry and Physics Discussions

from biomass burning, and is closely correlated with CO and HCN emissions (Notholt et al. 2000; Rinsland et al. 2002; Vigouroux et al. 2012; Zeng et al. 2012).

C_2H_6 is one of the target gases of a global ground-based Fourier transform infrared spectroscopy (FTIR) network, namely the Network for Detection of Atmospheric Composition Change (NDACC) (De Mazière et al. 2018). FTIR time series of C_2H_6 with different time periods have been reported in many stations for validation of satellite data or chemical model simulation (Abad et al. 2011; Franco et al. 2015; Franco et al. 2016; Glatthor et al. 2009), or evaluation of local air quality and air pollutants transport caused by anthropogenic emission and biomass burning (Angelbratt et al. 2011; Lutsch et al. 2016; Lutsch et al. 2019; Nagahama and Suzuki 2007; Rinsland et al. 2002; Simpson et al. 2012; Viatte et al. 2015; Viatte et al. 2014; Vigouroux et al. 2012; Zeng et al. 2012; Zhao et al. 2002). Several FTIR sites have observed the decrease in C_2H_6 over 1990 – 2010, and characterized consistent interannual trends in the −1 to −2.7% yr^{-1} range (Franco et al. 2015; Franco et al. 2016; Simpson et al. 2012; Zeng et al. 2012). This declining trend has been largely attributed to the reduction of global fugitive emissions (Franco et al. 2015; Simpson et al. 2012). Recently, several studies concluded that the long-term decline in C_2H_6 in the NH reversed from 2009 onwards (Franco et al. 2015; Franco et al. 2016). Using ground-based FTIR C_2H_6 total columns derived at five selected NDACC sites, Franco et al. (2016) characterized the C_2H_6 evolution from 2009 – 2015 and determined growth rates of ~3% yr^{-1} at remote sites and of ~5% yr^{-1} at mid-latitudes. This change is mainly attributed to the exploitation of shale gas and tight oil reservoirs in North America (Franco et al. 2016; Helmig et al. 2016).

The NDACC network has been operating for almost three decades around the globe (De Maziere et al. 2018; Sun et al. 2018a). However, most instruments are located in Europe and Northern America, but the number of observation sites in the rest parts of world remains sparse, and there is only one qualified observations site in China, i.e., the Hefei site (117°E, 32°N, 30 m a.s.l.) located in a densely populated and industrialized area in eastern China (Sun et al. 2018a). The Hefei site is not yet affiliated to the NDACC network but its observation routine is following the NDACC standard convention since 2015 (Sun et al. 2018a). As the consequence of a series of actions for emission control, air pollution over China in recent years has been significantly improved (Zhang et al. 2019; Zheng et al. 2018). However, the atmospheric pollution over densely populated and industrialized eastern China is still in severe situation (Zhang et al. 2019; Zheng et al. 2018). The complexity, extension, and severity of the atmospheric pollution in eastern China are still unrivaled compared to the rest of world (Lu et al. 2018; Zheng et al. 2018). FTIR observations at Hefei have been used extensively for evaluation of satellite data (Tian et al. 2018; Wang et al. 2017), chemical model simulation (Tian et al. 2018; Yin et al. 2020; Yin et al. 2019), local air quality (Shan et al. 2019; Sun et al. 2018a) and the transport of air pollutants caused by anthropogenic and biomass burning emissions (Sun et al. 2018a; Sun et al. 2020a; Sun et al. 2020b).

In this study, we first present and quantify the variability, source, and transport of C_2H_6 over densely populated and industrialized eastern China by using FTIR observation, GEOS-Chem model simulation, and atmospheric circulation pattern techniques. The seasonality and interannual variability of C_2H_6 over Hefei, eastern China from 2015 – 2020 are investigated. The dependencies of C_2H_6 on meteorological and co-emitted gases (hereafter emission factors) are analyzed by using generalized additive models (GAMs)(Wood and Simon 2004). The ground-based FTIR C_2H_6 time series are for the first time applied to evaluate the GEOS-Chem model for the specifics of C_2H_6 simulation over eastern China. We further run a series of GEOS-Chem sensitivity simulations to

https://doi.org/10.5194/acp-2021-13
Preprint. Discussion started: 22 March 2021

Atmospheric Chemistry and Physics Discussions

quantify relative contributions of various source categories and regions to the observed C_2H_6 abundance. The three-dimensional (3D) transport inflow and outflow pathways of C_2H_6 over the observation site are finally determined by the GEOS-Chem sensitivity simulations and atmospheric circulation pattern. This study can not only enhance the understanding of regional emission, transport, and air clean actions over eastern China, but also contribute to form new reliable remote sensing data in this sparsely-monitored regions for climate change research.

The next section describes the retrieval for FTIR tropospheric column-averaged dry-air mole fraction (troDMF) of C_2H_6, the configuration of GEOS-Chem model simulation, and the GAMs regression approach. Section 3 reports the variability of C_2H_6 troDMF and comparison with the GEOS-Chem simulation. Section 4 reports the GAMs regression results and the interpretation. Section 5 reports the results for source attribution using GEOS-Chem sensitivity simulation and atmospheric circulation pattern. We conclude the study in Section 6.

2. Methods and data

2.1 C_2H_6 troDMF retrieval

The C_2H_6 troDMF time series were calculated by using direct solar absorption spectra saved with a FTIR spectrometer in operation at Hefei, eastern China (Sun et al. 2018a; Tian et al. 2018). Site description and instrumentation can be found in (Sun et al. 2018a). Briefly, the FTIR observatory includes a high resolution FTIR spectrometer (IFS125HR, Bruker) and a solar tracker (Solar Tracker-A 547, Bruker). This FTIR observatory alternately saved near infrared (NIR) and middle infrared (MIR) solar spectra in routine observations (Tian et al. 2018). The NIR and MIR spectra are saved with different spectral resolutions but both of them can be used to retrieve total columns and volume mixing ratio (VMR) profiles of a variety of trace gases in the atmosphere. The MIR spectra used in present work are saved with a spectral resolution of 0.005cm^{-1} following the requirements of NDACC standard convention (http://www.ndacc.org/, last accessed on 27 December 2020). The FTIR instrument is equipped with a KBr beam splitter, a filter centered at 2800 cm^{-1}, and an InSb detector for C_2H_6 measurements. The number of C_2H_6 measurements on each measurement day varied from 1 to 17 with an average of 6. In total, there were 743 days of qualified measurements between 2015 and 2020.

In this study, the VMR profile of C_2H_6 was first retrieved by using the SFIT4 algorithm updated from SFIT2 (Pougatchev et al. 1995) and implementing the optimal estimation method (Rodgers 2000). The C_2H_6 troDMF was then calculated by taking a weighting average of the C_2H_6 VMR profile and the air mass using a fixed tropospheric altitude. The C_2H_6 VMR profile was retrieved in a broad window of 2976 – 2978 cm^{-1}. The VMR profiles of CH_4 and H_2O and column of O_3 were also retrieved together with the C_2H_6 VMR profile for minimizing the atmospheric absorption interference. Spectroscopic absorption parameters of all gases are based on the atm16 line list from the compilation of Geoffrey Toon (Sun et al. 2020a). The *a priori* vertical profiles of temperature H_2O, and pressure were interpolated from the National Centers for Environmental Protection (NCEP) reanalysis data and the *a priori* vertical profiles of other gases were from the statistical averages of the Whole-Atmosphere Community Climate Model version 6 (WACCM) simulations from 1980 to 2020. The diagonal elements of the *a priori* covariance matrices $\mathbf{S}_a$ and the measurement noise covariance matrices $\mathbf{S}_\varepsilon$ were set to standard deviation (SD) of the WACCM simulations and the inverse square of the signal-to-noise ratio (SNR) of each spectrum, respectively (Franco et al. 2015).

https://doi.org/10.5194/acp-2021-13
Preprint. Discussion started: 22 March 2021

Atmospheric Chemistry and Physics Discussions

The non-diagonal elements of both $\mathbf{S}_a$ and $\mathbf{S}_\varepsilon$ were set to zero. The instrument line shape (ILS) of the FTIR instrument deduced from optical path alignment diagnosis with a low-pressure HBr cell was adopted in the retrieval (Hase 2012; Sun et al. 2018b).

For each retrieval, the averaging kernels reflect the sensitivity of the retrieved profile to the real profile. The area of the averaging kernels at a specific height is calculated as the sum of the elements of the corresponding averaging kernels (Pougatchev et al. 1995). It represents the fraction of the retrieval at that height which comes from the measurement rather than from the *a priori* information (Rodgers, 2000). A value close to unity at a specific height indicates that the retrieved profile at that height is nearly independent of the *a priori* profile and is thus from the measurement. The trace of the averaging kernel matrix is defined as degrees of freedom for signal (DOFS) and it quantifies the number of independent information in the retrieved profile. Fig. 1 shows the averaging kernels as well as their area, cumulative sum of DOFS, and VMR profile of randomly selected C_2H_6 retrieval at Hefei. Ground-based FTIR C_2H_6 observations at Hefei have a sensitivity of larger than 0.7 from ground to about 10 km altitude, indicating that the retrievals are mainly sensitive to the troposphere. This also means that the retrieved profile information below 10 km comes for more than 70% from the measurement, or in other words, that the *a priori* signal impacts the retrieval by less than 30% [Fig 1(a)]. The typical DOFS obtained at Hefei over the total atmosphere for C_2H_6 is 1.69 ± 0.29 (1σ), meaning that we can roughly provide two pieces of information on the vertical profile [Fig 1(b)]. The shape of the retrieved profile is heavily weighted toward the lower troposphere. As shown in Fig.1(c), the C_2H_6 concentration decreased by 72.7% with an increase in the height from surface to 2 km and kept decreasing slowly in the rest part of the atmosphere till approaching around zero in the stratosphere and above. The C_2H_6 partial column below 10 km accounted for 88.6% of C_2H_6 total column. This percentage is expected to show less seasonal variation since the shape of the retrieved profile is similar to the shape of the *a priori* profile due to the low DOFS [Fig. 1 (c)]. As a result, in subsequent analysis, the C_2H_6 VMRs averaged between the surface and 10 km are selected as representatives of C_2H_6 troDMF. The selected tropospheric layer (from surface up to 10 km) corresponds to 1.47 ± 0.2 (1σ) of DOFS and can be used with confidence. This selected layer is totally within the tropopause height (~ 16 km) at Hefei over four seasons (Sun et al. 2020b). The Hefei site is located in the northeastern margin of a GEOS-Chem grid cell [Fig. 2 and Table 3]. This selected layer also ensures the line of sights of all observations are totally within the same grid cell.

We calculated the error budget for C_2H_6 retrieval at Hefei following the formalism of Rodgers (2000), and separated all error components into systematic or random errors according to whether they vary steadily or randomly over consecutive measurements. The random, systematic, and the combined error budgets for the selected tropospheric layer (from surface up to 10 km) are summarized in Table 1. The input covariance matrix of temperature is based on the differences between Sonde and an ensemble of NCEP temperature profiles near Hefei, leading to 2 to 5 K in the troposphere and 3 to 7 K in the stratosphere. For each interfering gases, the corresponding covariance matrix is obtained with the WACCM v6 climatology. The input covariance matrix of measurement error is based on the inverse square of the SNR of each spectrum. We regularly use a low-pressure HBr cell to diagnose the misalignment of the FTIR spectrometer and to realign the instrument when indicated. The FTIR spectrometer at Hefei is assumed to be not far from the ideal condition, and the input uncertainties for zero level, background curvature, field of view, optical path difference, solar zenith angle, interferogram phase, and ILS are estimated to be 1%. For the

https://doi.org/10.5194/acp-2021-13
Preprint. Discussion started: 22 March 2021

Atmospheric Chemistry and Physics Discussions

C_2H_6 spectroscopic absorption coefficients, the line list in atm16 follows HITRAN 2012 (Rothman et al., 2013), and we use 5% for line intensity, pressure-, and temperature-broadening coefficients. For the retrieval parameter and smoothing error, the input covariance matrix are prescribed from the optimal estimation retrieval outputs. To estimate the retrieval error of C_2H_6 troDMF at Hefei, the elements of all gain matrices were set to zero for the altitudes outside the selected layer. The contributions of all error components to C_2H_6 troDMF retrieval at Hefei are summarized in Table 1. The dominant random errors are from temperature uncertainty (1.69%) and the zero level uncertainty (1.54%), and the dominant systematic error is from the line intensity uncertainty (5.12%). Total random and systematic errors are estimated to be 2.32% and 5.48%, respectively. Total retrieval error calculated as square root sum of the squares of total random and systematic errors is estimated to be 6.21%.

In order to exclude the measurements that seriously affected by instable weather conditions or by the *a priori* profile due to low measurement information content in less favourable observational conditions, e.g., around noontime when the probed atmosphere is thinner, or in summer when C_2H_6 is less abundant. The FTIR measurements saved with a solar intensity variation (SIV) of larger than 10% or retrievals with total DOFS of less than 0.7 or the root-mean-square (RMS) of fitting residuals of larger than 2%, which accounted for 11.2% of total measurements, were excluded in this study.

2.2 GEOS-Chem sensitivity simulation

Relative contribution of various source categories and regions to the observed C_2H_6 abundance were quantified by a series of sensitivity simulations using the GEOS-Chem chemical model version 12.2.1 (Bey et al. 2001) (http://geos-chem.org, last access on 24 August 2020). All simulations implemented a universal tropospheric-stratospheric Chemistry (UCX) mechanism (Eastham et al. 2014; Fisher et al. 2017) and were driven by the Goddard Earth Observing System-Forward Processing (GEOS-FP) meteorological fields at a degraded horizontal resolution of 2◦×2.5◦. The temporal resolutions are 1 hour (hr) for surface variables and boundary layer height, and 3 hr for other variables. Dry deposition was calculated by the resistance-in-series algorithm (Wesely 1989; Zhang et al. 2001) and wet deposition followed that of Liu et al. (2001). The photolysis rates were available from the FAST-JX v7.0 photolysis scheme (Bian and Prather 2002). All simulations were spun up for one year (July 2014 to July 2015) and output hourly mean C_2H_6 VMR profiles globally ranging from the surface to 0.01 hPa at a horizontal resolution of 2◦×2.5◦. This study only considered the C_2H_6 simulations from 2015 to 2020 in the grid box containing Hefei (31.52°–32.11°N by 116.53°–118.02°E).

In the recent past, the inventories led to significant underestimation of the C_2H_6 simulation (e.g., HTAP2 in Franco et al. 2016). Since then, some efforts have improved the situation (e.g., Tzompa-Sosa et al. 2017). In this study, we refer to Sun et al. (2020a) for more details on implementation of emission inventories. Briefly, global anthropogenic emissions were from the Community Emissions Data System (CEDS) inventory which overwrites Asia by the latest Multi-resolution Emission Inventory for China (MEIC) (Hoesly et al. 2018; Li et al. 2017; Lu et al. 2019; Zheng et al. 2018). Global biomass burning and biogenic emissions were from the Global Fire Emissions Database (GFED v4) inventory (Giglio et al. 2013) and the Model of Emissions of Gases and Aerosols from Nature (MEGAN version 2.1) inventory (Guenther et al. 2012), respectively. The CH_4 emission fields are prescribed based on NOAA measurements for 1983–2016 and are

https://doi.org/10.5194/acp-2021-13
Preprint. Discussion started: 22 March 2021

Atmospheric Chemistry and Physics Discussions

extended to 2020 using the linear extrapolation of local 2011–2016 change rates (Murray, 2016; Lu et al., 2019).

Particular improvements have been done for the latest bottom-up MEIC emission inventory in the accuracy of vehicle emission modelling (Zheng et al. 2014), power plant emission calculation (Liu et al. 2015), and the non-methane VOCs (NMVOCs) speciation method (Li et al. 2014). Many studies have verified that the MEIC emission inventory can reasonably represents the anthropogenic emissions over Asia (Hoesly et al. 2018; Li et al. 2017; Lu et al. 2019; Sun et al. 2020a; Tian et al. 2018; Yin et al. 2020; Yin et al. 2019; Zheng et al. 2018). Anthropogenic C_2H_6 emissions in China by region and category for the 2015 and 2019 MEIC emission inventories are summarized in Table 2. All subdivided geographical regions are shown in Fig. 2 and the resulting delimitations are summarised in Table 3. The delimitations of these geographical regions are based on the levels of urbanization and industrialization in China. Region ① in Fig. 2 only covers a few sparsely city clusters representing the region with least population and industrialization in China (Lu et al. 2019). Regions ②, ④, and ⑤ cover the North China Plain (NCP), Yangtze River Delta (YRD), and Pearl River Delta (PRD) city clusters, respectively, which are the three most developed city clusters facing severe air pollution in China. Region ③ covers the Sichuan Basin (SCB) and central Yangtze River (CYR) city clusters with newly emerging severe air pollution in China. Total annual Chinese anthropogenic emissions of C_2H_6 in 2015 and 2019 are 0.883 Tg and 0.859 Tg, respectively. In both years, anthropogenic C_2H_6 emissions in China are dominated by industry and residential emissions. The highest anthropogenic C_2H_6 emission rates (calculated as the ratio of total C_2H_6 emission to the coverage) are in densely populated and industrialized region clusters in eastern part of China (including northern China (NR), eastern China (ER), central China (CR), southern China (SR), and adjacent regions) with little seasonal variation [Fig.A1]. The anthropogenic emissions in WR region are typically lower than those in other parts of China because of lower population and industries in the region (Lu et al. 2019; Zheng et al. 2018).

In order to quantify the contributions of different source categories and regions to the observed C_2H_6, we first conducted a reference full chemistry simulation (BASE) with implementation of all emission inventories as described above. Then, we conducted a series of sensitivity simulations to assess the change of each sensitivity simulation relative to the BASE simulation. Model configurations in this study were similar to those in Sun et al. (2020a) but with a different emission perturbation method. When an emission inventory was shut off in Sun et al. (2020a), the emissions of all atmospheric compounds in that inventory were suppressed. In contrast, this work only suppressed C_2H_6 in each case except for biogenic and biomass burning emission perturbations, which suppressed all atmospheric compounds since we cannot separate C_2H_6 emission from current biogenic and biomass burning emission inventories. Model configurations in this study are summarised in Table 3 and were described as follows.

(i) To analyse the contributions of different emission categories, we shut off C_2H_6 in each individual emission inventory to evaluate the change of the simulation in the presence of C_2H_6 in other emission inventories. As a result, the relative contribution of each emission category was estimated as the relative difference between the GEOS-Chem simulation in the presence and absence of C_2H_6 in that emission inventory. We have conducted four such sensitivity simulations by shutting off C_2H_6 emissions in (1) fossil fuel emission inventory (including emissions from agriculture, industry, power plant, residential, and transport), (2) biogenic emission inventory, (3) biomass burning emission inventory, and (4) biofuel emission inventory (Table 3). The sum of fossil

https://doi.org/10.5194/acp-2021-13
Preprint. Discussion started: 22 March 2021

Atmospheric Chemistry and Physics Discussions

fuel and biofuel C_2H_6 emissions is defined as anthropogenic C_2H_6 source and the sum of biogenic and biomass burning C_2H_6 emissions is referred to as natural C_2H_6 source.

(ii) To analyse the contributions of different geographical regions, we shut off all categories of C_2H_6 emissions (i.e., the aforementioned anthropogenic plus natural C_2H_6 sources) within each geographical region to assess the change of the simulation in the presence of C_2H_6 emissions outside that geographical region. Thus, the relative contribution of each geographical region was estimated as the relative difference between the GEOS-Chem simulation in the presence and absence of C_2H_6 emissions within that geographical region. We have conducted five such sensitivity simulations by shutting off C_2H_6 emissions within five geographical regions shown in Fig. 2.

2.3 Generalized additive models (GAMs) regression

In this study, we investigate the dependencies of C_2H_6 on meteorological and emission factors by using the GAMs regression (Wood and Simon 2004; Wood 2004). Regression analysis is proceeded using the thin plate smoothing spline function (Pearce et al. 2011). Smoothing parameters and confidence intervals are calculated according to the Restricted Maximum Likelihood standard (REML) and the unconditional Bayesian method, respectively (Pearce et al. 2011). The GAMs regression is better than the traditional statistical models in dealing with nonlinear fittings (Veaux and Richard 2012). For climate change applications, where there are many non-linear relationships between variables, the GAMs regression is particularly attractive (Zhang et al. 2019).

We introduced a variety of potential meteorological and emission factors into the GAMs regression one at a time and performed significance tests based on the Akaike's Information Criteria (AIC) values (Wood and Simon 2004). The explanatory variables which passed the significance tests with the smallest AIC values were included into the final GAMs model. Furthermore, explanatory variables in GAMs regression may interact with each other and result in unstable fittings due to the internal multicollinearity. For the explanatory variables that show a strong collinearity with each other, we only included one of them in the final GAMs model. The degree of multicollinearity can be quantified by the variance inflation factor (VIF) (Ma et al. 2020). Generally, a stronger collinearity between the explanatory variables results in a larger VIF, and the VIF of an explanatory variable could be 1.0 if it is not correlated with other explanatory variables (Ma et al. 2020). In this study, we included all the meteorological and emission factors in the GAMs and calculated the VIF for all the influencing factors. The multicollinearity diagnosis concluded that the main causes of multicollinearity are between the HCN and CO, and between the tropopause height and planetary boundary layer height (PBLH). Including either of these two data pairs in the GAMs regression showed significant collinearities with the VIF values of greater than an empirical threshold of 4.0, indicating an unstable regression (Lin et al. 2018). After omitting HCN and PBLH in the final GAMs model, the adjusted VIF values of all the variables were less than 4.0 and the variables uniformly passed the significance tests. As a result, the final GAMs model in the context of the C_2H_6 troDMF time series y can be described as (Pearce et al. 2011):

$$\log(y) = \beta + S(ua) + S(va) + S(omega) + S(qv) + S(troph) + S(pres) + S(temp) + S(ch_4) + S(co) + \varepsilon \quad (1)$$

where β and ε are the mean response constant and the fitting residual, respectively. $S(ua)$, $S(va)$, $S(omega)$, $S(qv)$, $S(troph)$, $S(pres)$, $S(temp)$, $S(ch_4)$, and $S(co)$ are the smoothing functions of daily average zonal wind (with a unit of m s^{-1}), meridional wind (m s^{-1}), vertical wind (Pa s^{-1}), water vapor

https://doi.org/10.5194/acp-2021-13
Preprint. Discussion started: 22 March 2021

Atmospheric Chemistry and Physics Discussions

concentration (%), tropopause height (km), pressure (hPa), temperature (°C), CH_4 troDMF (ppbv), and CO troDMF (ppbv). Positive values of *ua*, *va*, and *omega* represent northward, eastward, and upward winds, respectively. The sum of *S*(*ch*$_4$) and *S*(*co*) is referred to as the emission influences, and the sum of remaining smoothing functions is referred to as the meteorological influences.

For driving the GAMs regression, we first derived CH_4 and CO VMR profiles from direct solar absorption spectra similar to that of C_2H_6, see section 2.1. The spectra for CH_4 retrievals are exactly the same as those of C_2H_6 but the spectra for CO are saved at a different filter channel. The respective VMR profiles were then converted to troDMF values following the method of C_2H_6. The retrieval configurations, waveband selections and the interfering gases considerations for CH_4 and CO can be found in Sun et al. (2018b). The DOFS of the retrievals between surface and 10 km altitude for both CH_4 and CO are larger than 1.5 and the corresponding retrieval errors are less than 8% (Sun et al., 2018b). All meteorological factors are from the GEOS-FP meteorological fields at their native resolution of 0.25° × 0.3125° ranging from the surface to 0.01 hPa at a temporal resolution of 1 hr. Since the meteorological fields and C_2H_6 concentration are not uniformly distributed along the altitude, the summing mean values of the meteorological fields cannot properly characterize the meteorological influences. In this study, we use a method similar to that of Shaiganfar et al. (2017) to increase the influence weighting toward lower troposphere. As a result, all meteorological parameters except tropopause height (*troph*) are converted into the C_2H_6 profile weighting averaged value ω_{avg} through Eq. (2):

$$\omega_{avg} = \frac{\sum_i \boldsymbol{\omega}(z_i) \cdot \boldsymbol{c}(z_i) \cdot \boldsymbol{Airmass}(z_i)}{\sum_i \boldsymbol{c}(z_i) \cdot \boldsymbol{Airmass}(z_i)} \quad (2)$$

where $\boldsymbol{\omega}(z_i)$, $\boldsymbol{c}(z_i)$, and $\boldsymbol{Airmass}(z_i)$ represent the value of the meteorological factor, C_2H_6 concentration, and the air mass at the altitude z_i.

3. Variability and comparison with GEOS-Chem model data

We have compared the observed daily mean time series and seasonal cycle of C_2H_6 troDMF to the GEOS-Chem BASE simulations for investigating the chemical model performance for the specifics of polluted regions over eastern China. As the vertical resolution of GEOS-Chem is different from the FTIR observation, smoothing correction has been done for the GEOS-Chem profiles (Rodgers and Connor 2003). First, the GEOS-Chem daily mean profiles of C_2H_6 have been interpolated to the FTIR altitude grid for ensuring a common altitude grid. In order to match the FTIR observations which only operates during daytime, the average for GEOS-Chem simulations was only performed during daytime from 9:00 to 17:00 local time (LT). The interpolated profiles were then smoothed by the concurrent seasonal mean values of the FTIR averaging kernels and *a priori* profiles (Rodgers 2000; Rodgers and Connor 2003). The smoothed GEOS-Chem profiles were subsequently converted to troDMF values by using the corresponding regridded air density profiles from the model with the method described in section 2.1. Finally, the GEOS-Chem C_2H_6 troDMF time series only for the days with available FTIR observations were averaged by month and compared with the FTIR monthly mean data.

Fig. 3 (a) shows the comparison of daily mean time series of C_2H_6 troDMF between the FTIR observation and the smoothed GEOS-Chem model simulation from 2015 to 2020. Fig. 3 (b) compares the seasonal cycles derived from Fig. 3 (a) for the days with available FTIR observations only. Generally, the measured features in terms of seasonality and interannual variability can be

https://doi.org/10.5194/acp-2021-13
Preprint. Discussion started: 22 March 2021

Atmospheric Chemistry and Physics Discussions

reproduced by the GEOS-Chem simulations with a correlation coefficient (r) of 0.88. Large GEOS-Chem vs. FTIR differences tended to occur in the trough and peak of the observations. For instance, the observed monthly mean value of C_2H_6 troDMF was overestimated by 35.6% in July and overestimated by 17.4 % in December by the GEOS-Chem. These discrepancies may be mainly attributed to uncertainties in the horizontal transport and vertical mixing schemes simulated by the GEOS-Chem model at a relatively coarse spatial resolution, which are difficult to match column observation over a single point. In addition, the number of C_2H_6 measurements at Hefei on each measurement day varied a wide range from 1 to 17 depending on the weather condition, but GEOS-Chem simulations are available consecutively by hour for the same day. This difference in the temporal resolution of GEOS-Chem and FTIR could also cause inconsistencies due to the high variability of atmospheric C_2H_6. However, considering the concurrent data pairs only (± 30 min), the averaged difference between GEOS-Chem and FTIR data (GEOS-Chem minus FTIR) is (−0.02 ± 0.05) ppbv (−1.6 ± 4.2) %, which is within the FTIR uncertainty budget. As a result, GEOS-Chem can simulate C_2H_6 concentration and variability for the specifics of polluted regions over eastern China. With improved emission inventories, previous studies have also found that global chemistry transport models were able to reproduce the absolute values as well as seasonal cycles of the ground-based FTIR C_2H_6 observations in the other parts of the world (Franco et al., 2015; Franco et al., 2016; Tzompa-Sosa et al. 2017).

As typically observed, the peak-to-peak amplitude of the modulation with respect to the monthly mean of C_2H_6 troDMF spanned a large range of −16.0% to 72.8% depending on season [Fig. 3 (b)]. The observed C_2H_6 troDMF roughly decreases over time for the first half of the year and increases over time for the second half of the year [Fig. 3 (b)]. High levels of C_2H_6 troDMF occur in the late autumn to early spring and low levels of C_2H_6 troDMF occur in late spring to early autumn. The observed C_2H_6 troDMF reached a minimum monthly mean value of (0.36 ± 0.26) ppbv in July and a maximum monthly mean value of (1.76 ± 0.35) ppbv in December. C_2H_6 troDMFs in December were on average 4.9 times higher than those in July. Since the tropospheric OH oxidation capability in summer is higher than that in winter, the C_2H_6 seasonality characterized by a winter maximum and a summer minimum was also observed in other FTIR stations (Angelbratt et al. 2011; Franco et al. 2015; Franco et al. 2016; Lutsch et al. 2019; Nagahama and Suzuki 2007; Rinsland et al. 2002; Simpson et al. 2012; Viatte et al. 2015; Viatte et al. 2014; Vigouroux et al. 2012; Zeng et al. 2012; Zhao et al. 2002). We have used the bootstrap resampling method of Gardiner et al. (2008) to evaluate the seasonality and interannual variability of C_2H_6 troDMF, where a 3rd Fourier series plus a linear function was used to fit daily mean time series of C_2H_6 troDMF by both FTIR observations and GEOS-Chem model simulations. We incorporated the errors arising from the autocorrelation in the residuals into the uncertainties in the change rates following the procedure of Santer et al. (2008). The observed C_2H_6 troDMFs from 2015 to 2020 showed a negative change rate of (−2.60 ± 1.34)% yr^{-1}, which is in reasonable agreement with the modelled change rate of (−2.1 ± 0.7)% yr^{-1} [Fig. 3 (a)].

4. GAMs regression results and interpretation

C_2H_6 troDMF time series from 2015 to 2020 over Hefei by the FTIR and the GAMs regression model are shown in Fig. 4. The observed C_2H_6 variability can be reproduced by the GAMs regression model with a good agreement, as confirmed by a correlation coefficient (r) of 0.90 [Fig.

https://doi.org/10.5194/acp-2021-13
Preprint. Discussion started: 22 March 2021

Atmospheric Chemistry and Physics Discussions

4(a)]. Meanwhile, the observed C_2H_6 troDMF time series also show high correlations with both the accumulated meteorological factor (r=0.88) [Fig. 4 (b)] and the accumulated emission factor (r = 0.70) [Fig. 4(c)], indicating both meteorological and emission influences are important factors for driving the C_2H_6 troDMF variability. Generally, both meteorological and emission factors show positive influences on C_2H_6 troDMFs in cold season (DJF/MAM) and negative influences on C_2H_6 troDMFs in warm season (JJA/SON). However, the seasonal dependency of meteorological influence is stronger than that of emission influence. During the studied years, the year to year differences in meteorological influence are small, while the positive emission influence showed an overall decreasing change rate since 2016, which probably drives a decreasing change rate in C_2H_6 troDMF in recent years.

The influence of each explanatory variable x_i in GAMs regression calculated as $100\%\cdot[e^{s(x_i)}-1]$ are shown in Fig. 5, which reflects the influence of each individual variable on the relative change of C_2H_6 troDMF. The corresponding DOFS of each smoothing function are also shown in Fig.5. If an explanatory variable is linearly correlated with the C_2H_6 troDMF, the DOFS of the resulting smoothed variable could be equal to 1, and the larger the slope the higher the linear response. Otherwise, the larger the deviation of DOFS relative to 1, the more significant the nonlinear relationship is (Veaux and Richard 2012). During the studied years, the DOFS of zonal wind (*ua*), convection wind (*omega*), pressure (*pres*), tropopause height (*troph*), temperature (*temp*), and CO troDMF (*co*) were close to 1, reflecting a roughly linear relationship of these explanatory variables with the C_2H_6 troDMF. In contrast, the DOFS of meridional wind (*va*), H_2O troDMF (*qv*) and CH_4 troDMF (*ch₄*) were much greater than 1, reflecting a significant nonlinear relationship with the C_2H_6 troDMF.

The observed C_2H_6 troDMF was influenced by many factors. The zonal wind (*ua*), meridional wind (*va*), CH_4 troDMF (*ch₄*), and CO troDMF (*co*) showed positive influences and the other explanatory variables showed negative influences on the observed C_2H_6 troDMF variability. The results show that the northward, eastward, and downward convection winds facilitate the accumulation of C_2H_6 over the observation site and result in higher C_2H_6 troDMF. Since most anthropogenic and biomass burning sources of CO, and fossil fuel source of CH_4 are common sources of C_2H_6, C_2H_6 troDMF gradually went up as CH_4 and CO troDMFs increased. In contrast, meteorological conditions as high temperature, high humidity, and low pressure are more favorable to C_2H_6 oxidation, resulting in lower C_2H_6 troDMF. Meanwhile, deep upward convection wind and high tropopause height facilitate the diffusion of C_2H_6 over the observation site and result in lower C_2H_6 troDMF.

5. Source attribution

5.1 Contributions of different source categories and regions

The absolute and relative seasonal contributions of fossil fuel, biogenic, biomass burning, and biofuel emissions to C_2H_6 abundance from 2015 to 2020 over Hefei are shown in Fig. 6. The GEOS-Chem annual mean C_2H_6 troDMF simulations were decreased by 0.53, 0.26, 0.31, and 0.20 ppbv in the absence of fossil fuel, biogenic, biomass burning, and biofuel C_2H_6 emission inventories, which correspond to 34.5, 14.7, 22.4, and 14.7% of relative contribution to the modelled C_2H_6 abundance, respectively. The anthropogenic emissions account for 49.2% and the natural emissions account for 37.1% of the C_2H_6 abundance. The remaining contribution calculated as the difference between the

https://doi.org/10.5194/acp-2021-13
Preprint. Discussion started: 22 March 2021

Atmospheric Chemistry and Physics Discussions

BASE simulation and the sum of anthropogenic and natural contributions is 0.17 ppbv (13.7%). This missing rest can be largely attributed to nonlinear interactional effects among different sources which were not captured by the sensitivity simulations. Indeed, shutting off an emission inventory may induce significantly lower concentrations in atmospheric compounds (i.e., C_2H_6 for noFF and noBIOF or all suppressed compounds for noBVOC and noBB simulations) globally. On the one hand, some of them may react with OH, which would lead to higher OH concentrations available for the oxidation of C_2H_6, and eventually enhances the C_2H_6 destruction from other emission categories. On the other hand, some of them may form OH by a series of oxidation reaction, which would lead to lower OH concentrations available for the oxidation of C_2H_6, and eventually mitigates the C_2H_6 destruction from other emission categories. However, it is difficult to quantify the nonlinear impact of each individual emission category, since the concentration and spatial distribution of C_2H_6 in each emission category are different. Especially when biogenic and biomass burning emissions are suppressed, the impacts become hard to assess, since all NMVOCs compounds play a key role in both OH formation and destruction. Investigating the nonlinear impact of each individual emission category would require additional work that is beyond the scope of the present work.

The contributions of all emission sources are seasonal dependent, and the fossil fuel contribution shows the largest seasonal difference, which consolidates the GAMs regression results that the emission influences are seasonal dependent. The fossil fuel contribution in winter and spring (DJF/MAM) are larger than those in summer and autumn (JJA/SON), with a maximum of 52.0% in DJF and a minimum of 13.0% in JJA. The JJA/SON meteorological conditions which show stronger solar radiation, higher temperature, wetter atmospheric condition, and lower pressure than those in DJF/MAM are more favorable for increasing VOCs emissions from biogenic sources (BVOCs), which consolidates the fact that C_2H_6 abundance from biogenic source in JJA/SON are larger than those in DJF/MAM. The missing rest contributes to a maximum of 32% in JJA when the C_2H_6 oxidation reaches the seasonal maximum and is thus more sensitive to the on-off state of different sources.

Fig. 7 explores the absolute and relative seasonal contributions of ER, CR, NR, WR, and SR regions to the C_2H_6 abundance from 2015 to 2020 over Hefei. The GEOS-Chem annual mean C_2H_6 troDMF simulations were decreased by 0.28, 0.22, 0.29, 0.07, and 0.12 in the absence of the C_2H_6 emissions in ER, CR, NR, WR, and SR regions, which correspond to 21.5%, 15.8%, 20.3%, 5.7%, and 8.9%, of relative contribution to the modelled C_2H_6 abundance, respectively. The contributions of all geographical regions are also seasonal dependent. The results show that the observed C_2H_6 abundance was largely attributed to emissions within China (74.1%), which show a maximum in JJA/SON and a minimum in DJF/MAM. As vicinities of the observation site, the ER, CR, and NR regions dominated the contribution within China (57.6%). The remaining contribution calculated as the difference between the BASE simulation and the total contributions of above individual source regions is 0.42 ppbv (25.9%). This contribution is the sum of C_2H_6 emissions outside China (ROW) and the nonlinear interactional effects among the geographical sensitivity simulations. This rest contribution in DJF/MAM are ~ 4.0 times larger than those in JJA/SON. Considering the nonlinear interactional effects mainly occur in JJA/SON but this rest contribution in the meantime shows the seasonal minimum value, this remaining contribution can be largely attributed to ROW contributions.

As a relatively long lifetime species (a few months), C_2H_6 emissions originating from either

https://doi.org/10.5194/acp-2021-13
Preprint. Discussion started: 22 March 2021

Atmospheric Chemistry and Physics Discussions

nearby or in distant areas can be transported to Hefei site under favourable weather conditions, and thus contribute to the observed C_2H_6 abundance. In addition, atmospheric compounds originating either nearby or in distant areas, which affect the chemistry of C_2H_6 oxidation, could also affect the observed C_2H_6 abundance. For contributions within China, the lowest contribution of the WR region to the observed C_2H_6 abundance is largely attributed to the lowest C_2H_6 emission rates in this region (Table 2). A smaller contribution of the SR region to the observed C_2H_6 abundance in DJF/MAM in comparison with the ER, CR, and NR regions is mainly attributed to less air masses that originated in south China under the dry winter monsoon conditions, see section 5.2.

5.2 Transport inflow and outflow pathways

The direct GEOS-Chem sensitivity simulations can clearly characterize the 3D transport inflow and outflow pathways of C_2H_6 over the observation site. Fig.8 shows the spatial distribution of GEOS-Chem C_2H_6 BASE simulations around China along with horizontal wind vectors at 900 hPa in different seasons. General atmospheric circulation patterns over eastern China are typically affected by mid-latitude westerlies and Asian monsoon, including the East Asian summer monsoon and South Asian summer monsoon (Chen et al. 2009; Liang et al. 2005; Liu et al. 2003). Fig. 9 illustrates the latitude − height distributions of C_2H_6 VMR over China from six source regions along with the 3D atmospheric circulation patterns in different seasons. The 3D transport inflow and outflow pathways of C_2H_6 over the observation site are thus deduced as follows.

As indicated by the arrows in Figs. 8 and 9, the high pressure system over the Eurasian continent in DJF triggers the descending of strongly cold air over eastern China and results in air masses converging toward the observation site from western and northern areas, while the high pressure system over the Indian ocean and Pacific in JJA triggers the ascending of strongly heated air over eastern China and results in air masses converging toward the observation site from South Asia and East Asia (SEAS) (Liang et al. 2004; Liu et al. 2003). In DJF, the mid-latitude westerlies extend to tropics (about 15 °N) over middle and upper troposphere, and subtropics (about 30°N) near the surface, while the easterlies mainly prevail in tropics and are weak over eastern China [Figs. 8 and 9]. In the summer monsoon season, the atmospheric circulation patterns over eastern China change dramatically and is dominated by surface wind regime originating from Pacific, South China Sea, or Arabian Sea [Figs.8 and 9]. Meanwhile, the mid-latitude westerlies recede to the North Temperate Zone (north of 30°N) and the westerly jet center shifts to north of 50°N in JJA (from ~ 30°N in DJF) [Fig. 8]. In JJA, the tropical region is characterized by the strong easterlies in the upper troposphere and by the southwesterly air flow in the lower troposphere [Fig. 9]. The prevailing winds in the transition seasons in MAM and SON are still westerlies with frequent cold fronts [Figs. 8 and 9]. These above seasonal circulation patterns determine the transport inflow and outflow of C_2H_6 around the observation site. However, the transported scales are also influenced by source location and strength, travel trajectory and travel time (Liu et al. 2003).

Generally, C_2H_6 emissions from CR, NR, and WR regions can be transported to the observation site by the strong westerlies throughout the year [Fig. 9]. C_2H_6 from the SR region can be transported to the observation site by deep convection followed by northward transport into the mid-latitude westerlies in MAM or driven by the South Asian summer monsoon or westerlies in other seasons (Liu et al. 2003)[Fig. 8]. The observed C_2H_6 transport inflow originating from the local ER region is mainly driven by the local circulation cell or Asian monsoon. The driver for C_2H_6 transport inflow

https://doi.org/10.5194/acp-2021-13
Preprint. Discussion started: 22 March 2021

Atmospheric Chemistry and Physics Discussions

originating from the northern ROW (> 32°N) is the same as those from the CR, NR, and WR regions. The driver for C_2H_6 transport inflow originating from the southern ROW (< 32°N) is the same as that from the SR region. However, C_2H_6 originating from ROW relative to those from China reaches a higher altitude due to longer transport distances. The ROW contributions in JJA/SON are lower than those in DJF/MAM can be partly attributed to a stronger removal along the long-range transport pathway by the abundant wet precipitation and oxidation during the summer monsoon and post monsoon season.

Seasonal variability in C_2H_6 transport outflow over the observation site is mainly associated with the monsoon system. In DJF, C_2H_6 over the observation site is capped in the lower troposphere by the subsidence over eastern China and is swept by northeasterly southwestward into southwestern areas, where they are lifted up into the free troposphere by convection and then flow away northeastward [Fig. 9]. In JJA, the observed C_2H_6 is transported northeastward by the Asian monsoon and is undergone frequent lifting into the upper troposphere by deep convection [Figs. 8 and 9]. Frequent cold fronts are common phenomena during meteorologically transitional periods in MAM and SON. In SON, the winter monsoon builds continental high system, and sweeps the observed C_2H_6 in the lower troposphere northward to relatively high latitudes where they can be lifted up into the free troposphere by deep convection or cold fronts. In MAM, convection over lower latitudes at Asian continent starts to rise, which lifts up the observed C_2H_6 into the free troposphere and then flow away southward.

5.3 Potential factors driving interannual variability of C_2H_6

China has implemented a series of active clean air policies since 2013 to mitigate severe air pollution problems (Sun et al. 2020b; Zhang et al. 2019; Zheng et al. 2018). Since then the emissions of major air pollutants have decreased, and the overall air quality has greatly improved (Sun et al. 2020b; Zhang et al. 2019; Zheng et al. 2018). Many air pollutants, such as NO_2, sulphur dioxide (SO_2), particulate matter 2.5 ($PM_{2.5}$), PM_{10}, CO, black carbon (BC), and organic carbon (OC), showed negative trends in recent years (Lu et al., 2019; Zhang et al. 2019; Zheng et al. 2018). We follow the method of Zheng et al. (2018) to estimate the relative change rate of anthropogenic C_2H_6 emissions in China during 2015 – 2019 using the MEIC emission inventory. As tabulated in Table 2, anthropogenic C_2H_6 emissions in all geographical regions showed a decreasing change rate during 2015 – 2019 except those in WR region where industrialization, urbanization, land use, and infrastructure construction have expanded rapidly in recent years, resulting in an increasing change rate of anthropogenic C_2H_6 emissions in the region (Ran et al. 2014). The relative change rates of anthropogenic C_2H_6 emissions in China during 2015 – 2019 are estimated as: 12.12% for WR, –5.32% for NR, –1.03% for CR, –7.66% for ER, –5.01% for SR, and –2.74% in total. The major driving forces for the decline in C_2H_6 emissions over China are attributed to the reductions from residential and transport sectors, with relative change rates of –14.53% and –3.53%, respectively (Table 2).

The interannual change rate of anthropogenic C_2H_6 emissions in China in recent years is estimated to be – 0.69% yr^{-1} (calculated as – 2.74%/(2019 – 2015)), which is much lower than the observed decreasing change rate in C_2H_6 tropDMF (−2.60 ± 1.34% yr^{-1}), indicating additional driving forces could exist, e.g., reductions in natural C_2H_6 emissions in China or reductions in long range transport of C_2H_6 emissions originating either anthropogenic or natural sources outside China.

https://doi.org/10.5194/acp-2021-13
Preprint. Discussion started: 22 March 2021

Atmospheric Chemistry and Physics Discussions

On the one hand, the Law of the People's Republic of China on the Prevention and Control of Atmospheric Pollution included the prohibition of crop residue burning over China in 2015 because crop residue burning emissions can result in poor air quality (http://www.chinalaw.gov.cn, last access on 19 June 2020). Since then the crop residue burning events over China decreased dramatically (Sun et al. 2020b). Meanwhile, biomass burning events in Africa, SEAS, and Oceania regions in 2015 were higher than those in onward years due to the El Niño Southern Oscillation (ENSO) (Sun et al. 2020b). The decreased global biomass burning emissions could probably also contribute to the observed decreasing change rate in C_2H_6 tropDMF over Hefei since 2015. On the other hand, large oil price fluctuations in recent years probably tightened oil and gas development around the globe which can cause a reduction in C_2H_6 leakage around the globe. However, C_2H_6 observations around the globe and more statistical data are needed to support this deduction, which is beyond the scope of this paper and requires further study.

6. Summary and conclusion

Ethane (C_2H_6) is an important greenhouse (GHG) gas and plays a significant role in tropospheric chemistry and climate change. As a relatively long residence time species (a few months), observations of C_2H_6 can reflect regional and hemispheric changes in emissions and climate, and can be assimilated into a chemical transport model to assess nonlocal emissions and provide valuable insights into model biases of C_2H_6 simulations.

This study for the first time presents and quantifies the variability, source, and transport of C_2H_6 over densely populated and industrialized eastern China by using ground-based high-resolution Fourier transform infrared (FTIR) observations. Seasonal and interannual variability of C_2H_6 over Hefei, eastern China from 2015 – 2020 have been investigated. The dependencies of C_2H_6 on meteorological and emission factors were analyzed by using generalized additive models (GAMs). The FTIR C_2H_6 time series are for the first time applied to evaluate the standard GEOS-Chem full-chemistry model for the specifics of C_2H_6 simulation over eastern China. GEOS-Chem model simulation with the state-of-the art inventory is in good agreement with the FTIR observation. The GEOS-Chem model was further run in a sensitivity mode to quantify relative contribution of various source categories and regions to the observed C_2H_6 abundance. The three-dimensional (3D) transport inflow and outflow pathways of C_2H_6 over the observation site were finally determined by the GEOS-Chem sensitivity simulation and atmospheric circulation pattern.

We obtained a retrieval error of 6.21 ± 1.2 (1σ)% and degrees of freedom (DOFS) of 1.47 ± 0.2 (1σ) in retrieval of C_2H_6 tropospheric column-averaged dry-air mole fraction (troDMF). The observed C_2H_6 troDMF reached a minimum monthly mean value of (0.36 ± 0.26) ppbv in July and a maximum monthly mean value of (1.76 ± 0.35) ppbv in December, and showed a negative change rate of (−2.60 ± 1.34) %/yr from 2015 to 2020. Generally, both meteorological and emission factors have positive influences on C_2H_6 troDMF in cold season (DJF/MAM) and negative influences in warm season (JJA/SON). GEOS-Chem model sensitivity simulations concluded that the anthropogenic emissions (fossil fuel plus biofuel) accounted for 49.2% and the natural emissions (biomass burning plus biogenic) accounted for 37.1% of C_2H_6 abundance over Hefei. The observed C_2H_6 abundance over Hefei was mainly attributed to the emissions within China (74.1%), where central, eastern, and northern China dominated the contribution (57.6%). Seasonal variability in C_2H_6 transport inflow and outflow over the observation site is largely related to the mid-latitude

https://doi.org/10.5194/acp-2021-13
Preprint. Discussion started: 22 March 2021

westerlies and Asian monsoon system. Reduction in C_2H_6 from 2015 to 2020 mainly results from the decrease in local and transported C_2H_6 emissions, which points to air quality improvement in China in recent years.

This study can not only enhance the insights of regional emission, transport, and air clean actions over China, but also contribute to form new reliable remote sensing dataset in this sparsely-monitored regions for climate change research.

Code and data availability. The new ground-based Fourier transform infrared (FTIR) spectroscopic remote sensing dataset for atmospheric C_2H_6 over Hefei, eastern China in this study can be accessed from https://doi.org/10.6084/m9.figshare.13020545. The MEIC emission inventories used in this study are available from http://meicmodel.org/.

Author contributions. YS designed and wrote the paper with inputs from all coauthors. HY carried out the GEOS-Chem simulations and GAMs regression. BZ provided the latest MEIC emission inventory. The rest authors contributed to this work by providing constructive comments.

Competing interests. The authors declare that they have no conflict of interest.

Acknowledgements. The processing and post processing environment for SFIT4 are provided by National Center for Atmospheric Research (NCAR), Boulder, Colorado, USA. The NDACC network is acknowledged for supplying the SFIT software. The LINEFIT code is provided by Frank Hase, Karlsruhe Institute of Technology (KIT), Institute for Meteorology and Climate Research (IMK-ASF), Germany. We thank the senate of Bremen, Germany for support. We thank the FTIR group at university of Wollongong, Australia for help in setting up and operating the FTIR spectrometer at Hefei. We thank the GEOS-Chem team and Tsinghua University, China for providing the latest MEIC inventory.

Financial support. This work is jointly supported by the National Key Research and Development Program of China (No.2019YFC0214802, No.2017YFC0210002, No. 2016YFC0203302, 2018YFC0213201, 2019YFC0214702, 2016YFC0200404), the National Science Foundation of China (No.41775025, No. 41575021, No. 51778596, No. 91544212, No. 41722501, No. 51778596), and the Sino-German Mobility programme (M-0036). Emmanuel Mahieu is a Senior Research Associate with the Fonds de la Recherche Scientifique -FNRS. His contribution has been primarily supported by the F.R.S.-FNRS under Grant no J.0147.18.

References

Abad, G. G., Allen, N. D. C., Bernath, P. F., Boone, C. D., McLeod, S. D., Manney, G. L., Toon, G. C., Carouge, C., Wang, Y., Wu, S., Barkley, M. P., Palmer, P. I., Xiao, Y., and Fu, T. M.: Ethane, ethyne and carbon monoxide concentrations in the upper troposphere and lower stratosphere from ACE and GEOS-Chem: a comparison study, Atmos. Chem. Phys., 11, 9927-9941, 2011.

Angelbratt, J., Mellqvist, J., Simpson, D., Jonson, J. E., Blumenstock, T., Borsdorff, T., Duchatelet, P.,

https://doi.org/10.5194/acp-2021-13
Preprint. Discussion started: 22 March 2021

Atmospheric Chemistry and Physics Discussions

Forster, F., Hase, F., Mahieu, E., De Maziere, M., Notholt, J., Petersen, A. K., Raffalski, U., Servais, C., Sussmann, R., Warneke, T., and Vigouroux, C.: Carbon monoxide (CO) and ethane (C_2H_6) trends from ground-based solar FTIR measurements at six European stations, comparison and sensitivity analysis with the EMEP model, Atmos. Chem. Phys., 11, 9253-9269, 2011.

Bey, I., Jacob, D. J., Yantosca, R. M., Logan, J. A., Field, B. D., Fiore, A. M., Li, Q. B., Liu, H. G. Y., Mickley, L. J., and Schultz, M. G.: Global modeling of tropospheric chemistry with assimilated meteorology: Model description and evaluation, J. Geophys. Res.-Atmos., 106, 23073-23095, 2001.

Bian, H. S., and Prather, M. J.: Fast-J2: Accurate simulation of stratospheric photolysis in global chemical models, J. Atmos. Chem., 41, 281-296, 2002.

Chen, D., Wang, Y., McElroy, M. B., He, K., Yantosca, R. M., and Le Sager, P.: Regional CO pollution and export in China simulated by the high-resolution nested-grid GEOS-Chem model, Atmos. Chem. Phys., 9, 3825-3839, 2009.

De Mazière, M., Thompson, A. M., Kurylo, M. J., Wild, J. D., Bernhard, G., Blumenstock, T., Braathen, G. O., Hannigan, J. W., Lambert, J. C., Leblanc, T., Mcgee, T. J., Nedoluha, G., Petropavlovskikh, I., Seckmeyer, G., Simon, P. C., Steinbrecht, W., and Strahan, S. E.: The Network for the Detection of Atmospheric Composition Change (NDACC): history, status and perspectives, Atmos. Chem. Phys., 18, 4935-4964, 2018.

Eastham, S. D., Weisenstein, D. K., and Barrett, S. R. H.: Development and evaluation of the unified tropospheric-stratospheric chemistry extension (UCX) for the global chemistry-transport model GEOS-Chem, Atmos. Environ., 89, 52-63, 2014.

Fischer, E. V., Jacob, D. J., Yantosca, R. M., Sulprizio, M. P., Millet, D. B., Mao, J., Paulot, F., Singh, H. B., Roiger, A., Ries, L., Talbot, R. W., Dzepina, K., and Deolal, S. P.: Atmospheric peroxyacetyl nitrate (PAN): a global budget and source attribution, Atmos. Chem. Phys., 14, 2679-2698, 2014.

Fisher, J. A., Murray, L. T., Jones, D. B. A., and Deutscher, N. M.: Improved method for linear carbon monoxide simulation and source attribution in atmospheric chemistry models illustrated using GEOS-Chem v9, Geosci. Model. Dev., 10, 4129-4144, 2017.

Franco, B., Bader, W., Toon, G. C., Bray, C., Perrin, A., Fischer, E. V., Sudo, K., Boone, C. D., Bovy, B., Lejeune, B., Servais, C., and Mahieu, E.: Retrieval of ethane from ground-based FTIR solar spectra using improved spectroscopy: Recent burden increase above Jungfraujoch, J. Quant. Spectrosc. Ra., 160, 36-49, 2015.

Franco, B., Mahieu, E., Emmons, L. K., Tzompa-Sosa, Z. A., Fischer, E. V., Sudo, K., Bovy, B., Conway, S., Griffin, D., Hannigan, J. W., Strong, K., and Walker, K. A.: Evaluating ethane and methane emissions associated with the development of oil and natural gas extraction in North America, Environ. Res. Lett., 11, 2016.

Gardiner, T., Forbes, A., de Maziere, M., Vigouroux, C., Mahieu, E., Demoulin, P., Velazco, V., Notholt, J., Blumenstock, T., Hase, F., Kramer, I., Sussmann, R., Stremme, W., Mellqvist, J., Strandberg, A., Ellingsen, K., and Gauss, M.: Trend analysis of greenhouse gases over Europe measured by a network of ground-based remote FTIR instruments, Atmos. Chem. Phys., 8, 6719-6727, 2008.

Giglio, L., Randerson, J. T., and van der Werf, G. R.: Analysis of daily, monthly, and annual burned area using the fourth-generation global fire emissions database (GFED4), J. Geophys. Res.-Biogeo., 118, 317-328, 10.1002/jgrg.20042, 2013.

Gilman, J. B., Lerner, B. M., Kuster, W. C., and de Gouw, J. A.: Source Signature of Volatile Organic Compounds from Oil and Natural Gas Operations in Northeastern Colorado (vol 47, pg 1297, 2013), Environ. Sci. & Tech., 47, 10094-10094, 2013.

https://doi.org/10.5194/acp-2021-13
Preprint. Discussion started: 22 March 2021

Atmospheric Chemistry and Physics Discussions

Glatthor, N., von Clarmann, T., Stiller, G. P., Funke, B., Koukouli, M. E., Fischer, H., Grabowski, U., Hopfner, M., Kellmann, S., and Linden, A.: Large-scale upper tropospheric pollution observed by MIPAS HCN and C_2H_6 global distributions, Atmos. Chem. Phys., 9, 9619-9634, 2009.

Guenther, A. B., Jiang, X., Heald, C. L., Sakulyanontvittaya, T., Duhl, T., Emmons, L. K., and Wang, X.: The Model of Emissions of Gases and Aerosols from Nature version 2.1 (MEGAN2.1): an extended and updated framework for modeling biogenic emissions, Geosci. Model. Dev., 5, 1471-1492, 2012.

Hase, F.: Improved instrumental line shape monitoring for the ground-based, high-resolution FTIR spectrometers of the Network for the Detection of Atmospheric Composition Change, Atmos. Meas. Tech., 5, 603-610, 2012.

Helmig, D., Rossabi, S., Hueber, J., Tans, P., Montzka, S. A., Masarie, K., Thoning, K., Plass-Duelmer, C., Claude, A., Carpenter, L. J., Lewis, A. C., Punjabi, S., Reimann, S., Vollmer, M. K., Steinbrecher, R., Hannigan, J., Emmons, L. K., Mahieu, E., Franco, B., Smale, D., and Pozzer, A.: Reversal of global atmospheric ethane and propane trends largely due to US oil and natural gas production, Nat. Geosci., 9, 490-495, 2016.

Hoesly, R. M., Smith, S. J., Feng, L. Y., Klimont, Z., Janssens-Maenhout, G., Pitkanen, T., Seibert, J. J., Vu, L., Andres, R. J., Bolt, R. M., Bond, T. C., Dawidowski, L., Kholod, N., Kurokawa, J., Li, M., Liu, L., Lu, Z. F., Moura, M. C. P., O'Rourke, P. R., and Zhang, Q.: Historical (1750-2014) anthropogenic emissions of reactive gases and aerosols from the Community Emissions Data System (CEDS), Geosci. Model. Dev., 11, 369-408, 2018.

Li, M., Zhang, Q., Streets, D. G., He, K. B., Cheng, Y. F., Emmons, L. K., Huo, H., Kang, S. C., Lu, Z., Shao, M., Su, H., Yu, X., and Zhang, Y.: Mapping Asian anthropogenic emissions of non-methane volatile organic compounds to multiple chemical mechanisms, Atmos. Chem. Phys., 14, 5617-5638, 2014.

Li, M., Zhang, Q., Kurokawa, J., Woo, J. H., He, K. B., Lu, Z. F., Ohara, T., Song, Y., Streets, D. G., Carmichael, G. R., Cheng, Y. F., Hong, C. P., Huo, H., Jiang, X. J., Kang, S. C., Liu, F., Su, H., and Zheng, B.: MIX: a mosaic Asian anthropogenic emission inventory under the international collaboration framework of the MICS-Asia and HTAP, Atmos. Chem. Phys., 17, 935-963, 2017.

Liang, Q., Jaegle, L., Jaffe, D. A., Weiss-Penzias, P., Heckman, A., and Snow, J. A.: Long-range transport of Asian pollution to the northeast Pacific: Seasonal variations and transport pathways of carbon monoxide, J. Geophys. Res.-Atmos., 109, 2004.

Liang, Q., Jaegle, L., and Wallace, J. M.: Meteorological indices for Asian outflow and transpacific transport on daily to interannual timescales, J. Geophys. Res.-Atmos., 110, 2005.

Lin, X., Liao, Y., and Hao, Y.: The burden associated with ambient $PM_{2.5}$ and meteorological factors in Guangzhou, China, 2012–2016: A generalized additive modeling of temporal years of life lost, Chemosphere, 212, 705-714, 2018.

Liu, F., Zhang, Q., Tong, D., Zheng, B., Li, M., Huo, H., and He, K. B.: High-resolution inventory of technologies, activities, and emissions of coal-fired power plants in China from 1990 to 2010, Atmos. Chem. Phys., 15, 13299-13317, 2015.

Liu, H. Y., Jacob, D. J., Bey, I., and Yantosca, R. M.: Constraints from Pb-210 and Be-7 on wet deposition and transport in a global three-dimensional chemical tracer model driven by assimilated meteorological fields, J. Geophys. Res.-Atmos., 106, 12109-12128, 2001.

Liu, H. Y., Jacob, D. J., Bey, I., Yantosca, R. M., Duncan, B. N., and Sachse, G. W.: Transport pathways for Asian pollution outflow over the Pacific: Interannual and seasonal variations, J. Geophys. Res.-Atmos., 108, 2003.

https://doi.org/10.5194/acp-2021-13
Preprint. Discussion started: 22 March 2021

Lu, X., Hong, J. Y., Zhang, L., Cooper, O. R., Schultz, M. G., Xu, X. B., Wang, T., Gao, M., Zhao, Y. H., and Zhang, Y. H.: Severe Surface Ozone Pollution in China: A Global Perspective, Environ. Sci. Tech. Let., 5, 487-494, 2018.

Lu, X., Zhang, L., Chen, Y. F., Zhou, M., Zheng, B., Li, K., Liu, Y. M., Lin, J. T., Fu, T. M., and Zhang, Q.: Exploring 2016-2017 surface ozone pollution over China: source contributions and meteorological influences, Atmos. Chem. Phys., 19, 8339-8361, 2019.

Lutsch, E., Dammers, E., Conway, S., and Strong, K.: Long-range transport of NH_3, CO, HCN, and C_2H_6 from the 2014 Canadian Wildfires, Geophys. Res. Lett., 43, 8286-8297, 2016.

Lutsch, E., Strong, K., Jones, D. B. A., Blumenstock, T., Conway, S., Fisher, J. A., Hannigan, J. W., Hase, F., Kasai, Y., Mahieu, E., Makarova, M., Morino, I., Nagahama, T., Notholt, J., Ortega, I., Palm, M., Poberovskii, A. V., Sussmann, R., and Warneke, T.: Detection and Attribution of Wildfire Pollution in the Arctic and Northern Mid-latitudes using a Network of FTIR Spectrometers and GEOS-Chem, Atmos. Chem. Phys. Discuss., 2019, 1-57, 10.5194/acp-2019-881, 2019.

Ma, Y. X., Ma, B. J., Jiao, H. R., Zhang, Y. F., Xin, J. Y., and Yu, Z.: An analysis of the effects of weather and air pollution on tropospheric ozone using a generalized additive model in Western China: Lanzhou, Gansu, Atmos. Environ., 224, 2020.

McKain, K., Down, A., Raciti, S. M., Budney, J., Hutyra, L. R., Floerchinger, C., Herndon, S. C., Nehrkorn, T., Zahniser, M. S., Jackson, R. B., Phillips, N., and Wofsy, S. C.: Methane emissions from natural gas infrastructure and use in the urban region of Boston, Massachusetts, P. Natl. Acad. Sci. USA, 112, 1941-1946, 2015.

Monks, S. A., Wilson, C., Emmons, L. K., Hannigan, J. W., Helmig, D., Blake, N. J., and Blake, D. R.: Using an Inverse Model to Reconcile Differences in Simulated and Observed Global Ethane Concentrations and Trends Between 2008 and 2014, J. Geophys. Res.-Atmos., 123, 11262-11282, 2018.

Nagahama, Y., and Suzuki, K.: The influence of forest fires on CO, HCN, C_2H_6, and C_2H_2 over northern Japan measured by infrared solar spectroscopy, Atmos. Environ., 41, 9570-9579, 2007.

Notholt, J., Toon, G. C., Rinsland, C. P., Pougatchev, N. S., Jones, N. B., Connor, B. J., Weller, R., Gautrois, M., and Schrems, O.: Latitudinal variations of trace gas concentrations in the free troposphere measured by solar absorption spectroscopy during a ship cruise, J. Geophys. Res.-Atmos., 105, 1337-1349, 2000.

Pearce, J. L., Beringer, J., Nicholls, N., Hyndman, R. J., and Tapper, N. J.: Quantifying the influence of local meteorology on air quality using generalized additive models, Atmos. Environ., 45, 1328-1336, 2011.

Pougatchev, N. S., Connor, B. J., and Rinsland, C. P.: Infrared Measurements of the Ozone Vertical-Distribution above Kitt Peak, J. Geophys. Res.-Atmos., 100, 16689-16697, 1995.

Ran, L., Lin, W. L., Deji, Y. Z., La, B., Tsering, P. M., Xu, X. B., and Wang, W.: Surface gas pollutants in Lhasa, a highland city of Tibet – current levels and pollution implications, Atmos. Chem. Phys., 14, 10721-10730, 10.5194/acp-14-10721-2014, 2014.

Rinsland, C. P., Jones, N. B., Connor, B. J., Wood, S. W., Goldman, A., Stephen, T. M., Murcray, F. J., Chiou, L. S., Zander, R., and Mahieu, E.: Multiyear infrared solar spectroscopic measurements of HCN, CO, C_2H_6,and C_2H_2 tropospheric columns above Lauder, New Zealand (45 degrees S latitude), J. Geophys. Res.-Atmos., 107, 2002.

Rodgers, C.: Inverse Methods for Atmospheric Sounding - Theory and Practice, in, 2000.

Rodgers, C. D., and Connor, B. J.: Intercomparison of remote sounding instruments, J. Geophys. Res.-

https://doi.org/10.5194/acp-2021-13
Preprint. Discussion started: 22 March 2021

Atmos., 108, Artn 411610.1029/2002jd002299, 2003.

Rothman, L. S., Gordon, I. E., Babikov, Y., Barbe, A., Benner,D. C., Bernath, P. F., Birk, M., Bizzocchi, L., Boudon,V., Brown, L. R., Campargue, A., Chance, K., Cohen, E. A.,Coudert, L. H., Devi, V. M., Drouin, B. J., Fayt, A., Flaud,J.-M., Gamache, R. R., Harrison, J. J., Hartmann, J.-M., Hill,C., Hodges, J. T., Jacquemart, D., Jolly, A., Lamouroux, J.,Roy, R. J. L., Li, G., Long, D. A., Lyulin, O. M., Mackie,C. J., Massie, S. T., Mikhailenk, S., Müller, H. S. P., Naumenko,O. V., and Nikitin, A. V.: The HITRAN2012 molecularspectroscopic database, J. Quant. Spectrosc. Ra., 130, 4–50, https://doi.org/10.1016/j.jqsrt.2013.07.002, 2013.

Roscioli, J. R., Yacovitch, T. I., Floerchinger, C., Mitchell, A. L., Tkacik, D. S., Subramanian, R., Martinez, D. M., Vaughn, T. L., Williams, L., Zimmerle, D., Robinson, A. L., Herndon, S. C., and Marchese, A. J.: Measurements of methane emissions from natural gas gathering facilities and processing plants: measurement methods, Atmos. Meas. Tech., 8, 2017-2035, 2015.

Santer, B. D., Thorne, P. W., Haimberger, L., Taylor, K. E., Wigley, T. M. L., Lanzante, J. R., Solomon, S., Free, M., Gleckler, P. J., Jones, P. D., Karl, T. R., Klein, S. A., Mears, C., Nychka, D., Schmidt, G. A., Sherwood, S. C., and Wentz, F. J.: Consistency of modelled and observed temperature trends in the tropical troposphere, Int. J. Climatol., 28, 1703-1722, 2008.

Shaiganfar, R., Beirle, S., van der Gon, H. D., Jonkers, S., Kuenen, J., Petetin, H., Zhang, Q., Beekmann, M., and Wagner, T.: Estimation of the Paris NO_x emissions from mobile MAX-DOAS observations and CHIMERE model simulations during the MEGAPOLI campaign using the closed integral method, Atmos. Chem. Phys., 17, 7853-7890, 2017.

Shan, C. G., Wang, W., Liu, C., Sun, Y. W., Hu, Q. H., Xu, X. W., Tian, Y., Zhang, H. F., Morino, I., Griffit, D. W. T., and Velazco, V. A.: Regional CO emission estimated from ground-based remote sensing at Hefei site, China, Atmos. Res., 222, 25-35, 2019.

Simpson, I. J., Andersen, M. P. S., Meinardi, S., Bruhwiler, L., Blake, N. J., Helmig, D., Rowland, F. S., and Blake, D. R.: Long-term decline of global atmospheric ethane concentrations and implications for methane, Nature, 488, 490-494, 2012.

Singh, H., Chen, Y., Staudt, A., Jacob, D., Blake, D., Heikes, B., and Snow, J.: Evidence from the Pacific troposphere for large global sources of oxygenated organic compounds, Nature, 410, 1078-1081, 2001.

Steinfeld, J. I.: Atmospheric Chemistry and Physics: From Air Pollution to Climate Change, Environment: Science and Policy for Sustainable Development, 40, 26-26, 10.1080/00139157.1999.10544295, 1998.

Sun, Y., Yin, H., Liu, C., Zhang, L., Cheng, Y., Palm, M., Notholt, J., Lu, X., Vigouroux, C., Zheng, B., Wang, W., Jones, N., Shan, C., Tian, Y., Hu, Q., and Liu, J.: Mapping the drivers of formaldehyde (HCHO) variability from 2015-2019 over eastern China: insights from FTIR observation and GEOS-Chem model simulation, Atmos. Chem. Phys. Discuss., 2020, 1-24, 10.5194/acp-2020-544, 2020a.

Sun, Y. W., Liu, C., Palm, M., Vigouroux, C., Notholt, J., Hui, Q. H., Jones, N., Wang, W., Su, W. J., Zhang, W. Q., Shan, C. G., Tian, Y., Xu, X. W., De Maziere, M., Zhou, M. Q., and Liu, J. G.: Ozone seasonal evolution and photochemical production regime in the polluted troposphere in eastern China derived from high-resolution Fourier transform spectrometry (FTS) observations, Atmos. Chem. Phys., 18, 14569-14583, 2018a.

Sun, Y. W., Palm, M., Liu, C., Hase, F., Griffith, D., Weinzierl, C., Petri, C., Wang, W., and Notholt, J.: The influence of instrumental line shape degradation on NDACC gas retrievals: total column and

https://doi.org/10.5194/acp-2021-13
Preprint. Discussion started: 22 March 2021

Atmospheric Chemistry and Physics Discussions

profile, Atmos. Meas. Tech., 11, 2879-2896, 2018b.

Sun, Y. W., Liu, C., Zhang, L., Palm, M., Notholt, J., Hao, Y., Vigouroux, C., Lutsch, E., Wang, W., Shan, C. G., Blumenstock, T., Nagahama, T., Morino, I., Mahieu, E., Strong, K., Langerock, B., De Maziere, M., Hu, Q. H., Zhang, H. F., Petri, C., and Liu, J. G.: Fourier transform infrared time series of tropospheric HCN in eastern China: seasonality, interannual variability, and source attribution, Atmos. Chem. Phys., 20, 5437-5456, 2020b.

Taylor, T. E., Eldering, A., Merrelli, A., Kiel, M., Somkuti, P., Cheng, C., Rosenberg, R., Fisher, B., Crisp, D., Basilio, R., Bennett, M., Cervantes, D., Chang, A., Dang, L., Frankenberg, C., Haemmerle, V. R., Keller, G. R., Kurosu, T., Laughner, J. L., Lee, R., Marchetti, Y., Nelson, R. R., O'Dell, C. W., Osterman, G., Pavlick, R., Roehl, C., Schneider, R., Spiers, G., To, C., Wells, C., Wennberg, P. O., Yelamanchili, A., and Yu, S.: OCO-3 early mission operations and initial (vEarly) XCO_2 and SIF retrievals, Remote Sens. Environ., 251, 112032, https://doi.org/10.1016/j.rse.2020.112032, 2020.

Tian, Y., Sun, Y. W., Liu, C., Wang, W., Shan, C. G., Xu, X. W., and Hu, Q. H.: Characterisation of methane variability and trends from near-infrared solar spectra over Hefei, China, Atmos. Environ., 173, 198-209, 2018.

Tzompa-Sosa, Z. A., Mahieu, E., Franco, B., Keller, C. A., Turner, A. J., Helmig, D., Fried, A., Richter, D., Weibring, P., Walega, J., Yacovitch, T. I., Herndon, S. C., Blake, D. R., Hase, F., Hannigan, J. W., Conway, S., Strong, K., Schneider, M., and Fischer, E. V.: Revisiting global fossil fuel and biofuel emissions of ethane, J. Geophys. Res.-Atmos., 122, 2493-2512, 2017.

Van Dingenen, R., Dentener, F. J., Raes, F., Krol, M. C., Emberson, L., and Cofala, J.: The global impact of ozone on agricultural crop yields under current and future air quality legislation, Atmos. Environ., 43, 604-618, 2009.

Veaux, D., and Richard, D.: Generalized Additive Models, Technometrics, 34, 225-226, 2012.

Viatte, C., Strong, K., Walker, K. A., and Drummond, J. R.: Five years of CO, HCN, C_2H_6, C_2H_2, CH_3OH, HCOOH and H_2CO total columns measured in the Canadian high Arctic, Atmos. Meas. Tech., 7, 1547-1570, 2014.

Viatte, C., Strong, K., Hannigan, J., Nussbaumer, E., Emmons, L. K., Conway, S., Paton-Walsh, C., Hartley, J., Benmergui, J., and Lin, J.: Identifying fire plumes in the Arctic with tropospheric FTIR measurements and transport models, Atmos. Chem. Phys., 15, 2227-2246, 2015.

Vigouroux, C., Stavrakou, T., Whaley, C., Dils, B., Duflot, V., Hermans, C., Kumps, N., Metzger, J. M., Scolas, F., Vanhaelewyn, G., Muller, J. F., Jones, D. B. A., Li, Q., and De Maziere, M.: FTIR time-series of biomass burning products (HCN, C_2H_6, C_2H_2, CH_3OH, and HCOOH) at Reunion Island (21 degrees S, 55 degrees E) and comparisons with model data, Atmos. Chem. Phys., 12, 10367-10385, 2012.

Wang, W., Tian, Y., Liu, C., Sun, Y. W., Liu, W. Q., Xie, P. H., Liu, J. G., Xu, J., Morino, I., Velazco, V. A., Griffith, D. T., Notholt, J., and Warneke, T.: Investigating the performance of a greenhouse gas observatory in Hefei, China, Atmos. Meas. Tech., 10, 2627-2643, 2017.

Wesely, M. L.: Parameterization of Surface Resistances to Gaseous Dry Deposition in Regional-Scale Numerical-Models, Atmos. Environ., 23, 1293-1304, 1989.

Wood, and Simon, N.: Stable and Efficient Multiple Smoothing Parameter Estimation for Generalized Additive Models, Journal of the American Statistical Association, 99, 673-686, 2004.

Wood, S. N.: Stable and efficient multiple smoothing parameter estimation for generalized additive models, Journal of the American Statistical Association, 99, 673-686, 2004.

Xiao, Y. P., Logan, J. A., Jacob, D. J., Hudman, R. C., Yantosca, R., and Blake, D. R.: Global budget of

https://doi.org/10.5194/acp-2021-13
Preprint. Discussion started: 22 March 2021

Atmospheric Chemistry and Physics Discussions

ethane and regional constraints on US sources, J. Geophys. Res.-Atmos., 113, 2008.

Yin, H., Sun, Y. W., Liu, C., Zhang, L., Lu, X., Wang, W., Shan, C. G., Hu, Q. H., Tian, Y., Zhang, C. X., Su, W. J., Zhang, H. F., Palm, M. A., Notholt, J., and Liu, J. G.: FTIR time series of stratospheric NO2 over Hefei, China, and comparisons with OMI and GEOS-Chem model data, Opt. Express, 27, A1225-A1240, 2019.

Yin, H., Sun, Y. W., Liu, C., Lu, X., Smale, D., Blumenstock, T., Nagahama, T., Wang, W., Tian, Y., Hu, Q. H., Shan, C. G., Zhang, H. F., and Liu, J. G.: Ground-based FTIR observation of hydrogen chloride (HCl) over Hefei, China, and comparisons with GEOS-Chem model data and other ground-based FTIR stations data, Opt. Express, 28, 8041-8055, 2020.

Zeng, G., Wood, S. W., Morgenstern, O., Jones, N. B., Robinson, J., and Smale, D.: Trends and variations in CO, C_2H_6, and HCN in the Southern Hemisphere point to the declining anthropogenic emissions of CO and C_2H_6, Atmos. Chem. Phys., 12, 7543-7555, 2012.

Zhang, C. X., Liu, C., Hu, Q. H., Cai, Z. N., Su, W. J., Xia, C. Z., Zhu, Y. Z., Wang, S. W., and Liu, J. G.: Satellite UV-Vis spectroscopy: implications for air quality trends and their driving forces in China during 2005-2017, Light-Sci. Appl., 8, 2019.

Zhang, L. M., Gong, S. L., Padro, J., and Barrie, L.: A size-segregated particle dry deposition scheme for an atmospheric aerosol module, Atmos. Environ., 35, 549-560, 2001.

Zhao, Y., Strong, K., Kondo, Y., Koike, M., Matsumi, Y., Irie, H., Rinsland, C. P., Jones, N. B., Suzuki, K., Nakajima, H., Nakane, H., and Murata, I.: Spectroscopic measurements of tropospheric CO, C_2H_6, C_2H_2,and HCN in northern Japan, J. Geophys. Res.-Atmos., 107, 2002.

Zheng, B., Huo, H., Zhang, Q., Yao, Z. L., Wang, X. T., Yang, X. F., Liu, H., and He, K. B.: High-resolution mapping of vehicle emissions in China in 2008, Atmos. Chem. Phys., 14, 9787-9805, 2014.

Zheng, B., Tong, D., Li, M., Liu, F., Hong, C. P., Geng, G. N., Li, H. Y., Li, X., Peng, L. Q., Qi, J., Yan, L., Zhang, Y. X., Zhao, H. Y., Zheng, Y. X., He, K. B., and Zhang, Q.: Trends in China's anthropogenic emissions since 2010 as the consequence of clean air actions, Atmos. Chem. Phys., 18, 14095-14111, 10.5194/acp-18-14095-2018, 2018.

https://doi.org/10.5194/acp-2021-13
Preprint. Discussion started: 22 March 2021

Atmospheric Chemistry and Physics Discussions

Tables

Table 1. Error budget and degrees of freedom (DOFS) for signal of randomly selected C_2H_6 troDMF retrieval at Hefei, eastern China

Error source	Input value	Error budget
Temperature uncertainty	1σ of NCEP	1.69%
Zero level uncertainty	1%	1.45%
Retrieval parameters uncertainty	*	< 0.1%
Measurement error	$1/SNR^2$	0.53%
Interfering species uncertainty	SD of WACCM	0.11%
Smoothing uncertainty	*	0.37%
Total random error	/	2.32%
Background curvature uncertainty	1%	0.14%
Field of view uncertainty	1%	< 0.1%
Optical path difference uncertainty	1%	< 0.1%
Solar zenith angle uncertainty	1%	< 0.1%
Phase uncertainty	1%	< 0.1%
ILS uncertainty	1%	< 0.1%
Line temperature broadening uncertainty	5%	0.4%
Line intensity uncertainty	5%	5.12%
Line pressure broadening uncertainty	5%	0.93%
Total systematic error	/	5.48%
Total errors	/	6.21%
DOFS (-)	/	1.47

* These input values for error budget estimation are based on the retrieval output

Table 2. Anthropogenic C_2H_6 emissions in China by region and category for the 2015 and 2019 MEIC emission inventories

Region		Industry (Tg yr^{-1})	Power plant (Tg yr^{-1})	Residential (Tg yr^{-1})	Transport (Tg yr^{-1})	Sum (Tg yr^{-1})
WR	2015	0.084	<0.01	0.011	<0.01	0.1
	2019	0.097	<0.01	0.011	<0.01	0.112
	change	15.36%	82.54%	− 6.61%	− 3.41%	12.12%
NR	2015	0.241	<0.01	0.125	0.026	0.394
	2019	0.241	<0.01	0.105	0.025	0.373
	change	0.04%	2.51%	− 15.96%	− 4.38%	− 5.32%
CR	2015	0.144	<0.01	0.041	<0.01	0.189
	2019	0.15	<0.01	0.033	<0.01	0.187
	change	4.68%	− 7.00%	–20.75%	− 1.13%	− 1.03%
ER	2015	0.07	<0.01	0.026	0.01	0.11
	2019	0.067	<0.01	0.022	0.01	0.097
	change	–4.83%	5.40%	–16.79%	− 3.70%	–7.66%
SR	2015	0.06	<0.01	0.026	0.01	0.09
	2019	0.056	<0.01	0.027	0.01	0.09
	change	− 7.94%	− 9.26%	1.52%	− 4.24%	− 5.01%
China	2015	0.60	<0.01	0.231	0.05	0.883
	2019	0.612	<0.01	0.197	0.048	0.859
	change	1.91%	4.04%	–14.53%	–3.93%	–2.74%

https://doi.org/10.5194/acp-2021-13
Preprint. Discussion started: 22 March 2021

Atmospheric Chemistry and Physics Discussions

1 **Table 3.** GEOS-Chem model configurations and delimitations of all geographical regions used in sensitivity
2 simulations.

Simulation	Region	Description
BASE	Global	Standard simulation with all anthropogenic and natural C_2H_6 emissions. The BASE simulation is taken as the reference and used for model evaluation
noFF	Global	Turn off global fossil fuel C_2H_6 emissions in BASE simulation
noBVOC	Global	Turn off global biogenic C_2H_6 emissions in BASE simulation
noBB	Global	Turn off global biomass burning C_2H_6 emissions in BASE simulation
noBIOF	Global	Turn off global biofuel C_2H_6 emissions in BASE simulation
Rest	Global	Difference between BASE and the sum of FF, BVOC, BB, and BIOF contributions
noWR	78.6° E – 103.4° E; 27.6°N - 48.8°N	Turn off fossil fuel, biogenic, biomass burning, and biofuel C_2H_6 emissions within western China (WR), i.e., region ① in Fig. 2, in BASE simulation
noNR	103.4°E – 129.8°E; 34.6°N – 53.5°N	Turn off fossil fuel, biogenic, biomass burning, and biofuel C_2H_6 emissions within northern China (NR), i.e., region ② in Fig. 2, in BASE simulation
noCR	103.4°E – 115.6°E; 27.6°N – 34.6°N	Turn off fossil fuel, biogenic, biomass burning, and biofuel C_2H_6 emissions within central China (CR), i.e., region ③ in Fig. 2, in BASE simulation
noER	115.6°E – 123.6°E; 21.0°N – 34.6°N	Turn off fossil fuel, biogenic, biomass burning, and biofuel C_2H_6 emissions within eastern China (ER), i.e., region ④ in Fig. 2, in BASE simulation
noSR	98.1°E – 115.6°E; 21.0°N – 27.6°N	Turn off fossil fuel, biogenic, biomass burning, and biofuel C_2H_6 emissions within southern China (SR), i.e., region ⑤ in Fig. 2, in BASE simulation
ROW	Rest of world	Difference between BASE and the sum of WR, NR, CR, ER, and SR contributions

3

4

https://doi.org/10.5194/acp-2021-13
Preprint. Discussion started: 22 March 2021

Atmospheric Chemistry and Physics Discussions

Figures

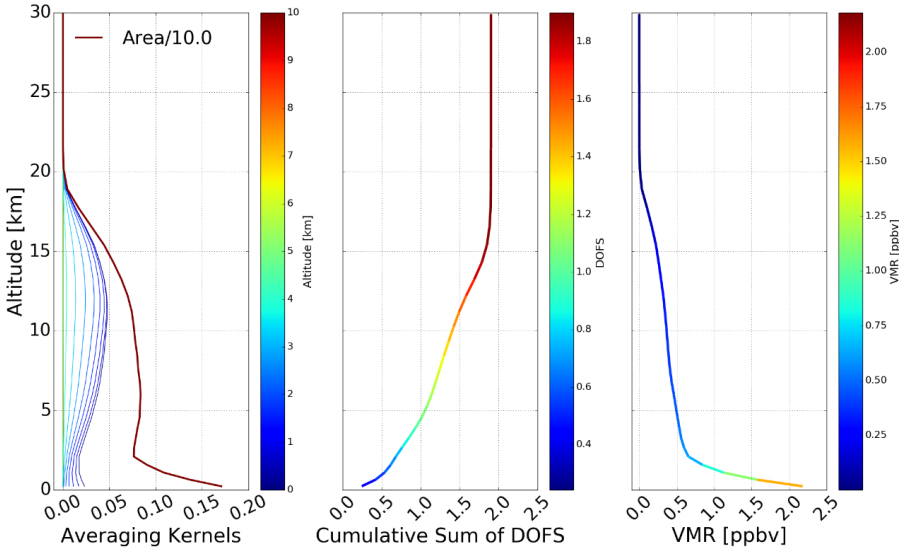

Fig. 1. Averaging kernels and their area scaled by a factor of 0.1, cumulative sum of degrees of freedom for signal (DOFS), and volume mixing ratio (VMR) profile of randomly selected C_2H_6 retrieval over Hefei, eastern China.

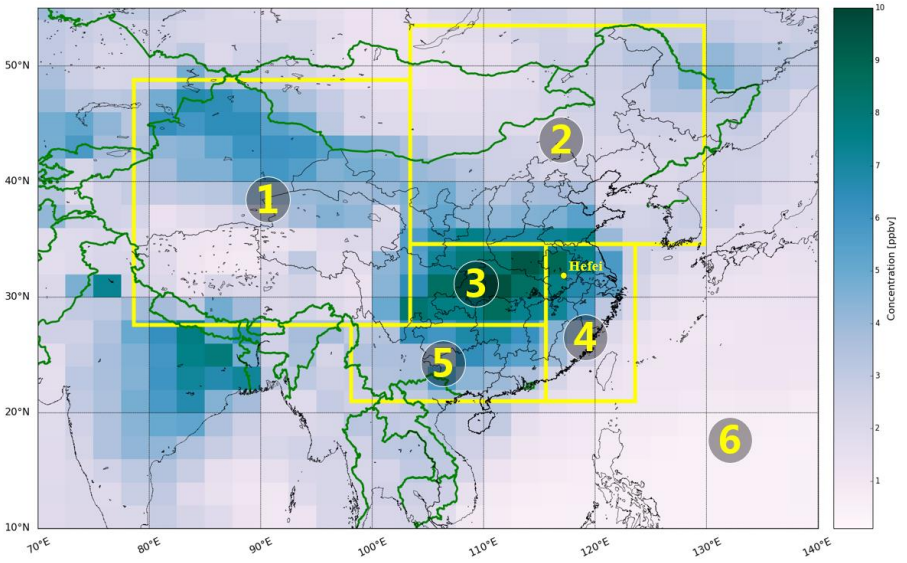

Fig. 2. Geographical regions used for GEOS-Chem sensitivity simulations. The numbers ①–⑥ represent western, northern, central, eastern, and southern China, and the rest of world, respectively. See Table 3 for latitude and longitude delimitations. Daily mean values of C_2H_6 troDMF on 1 January 2017 provided by GEOS-Chem BASE simulation was selected as a representative of wintertime enhancement in eastern China.

https://doi.org/10.5194/acp-2021-13
Preprint. Discussion started: 22 March 2021

Atmospheric Chemistry and Physics Discussions

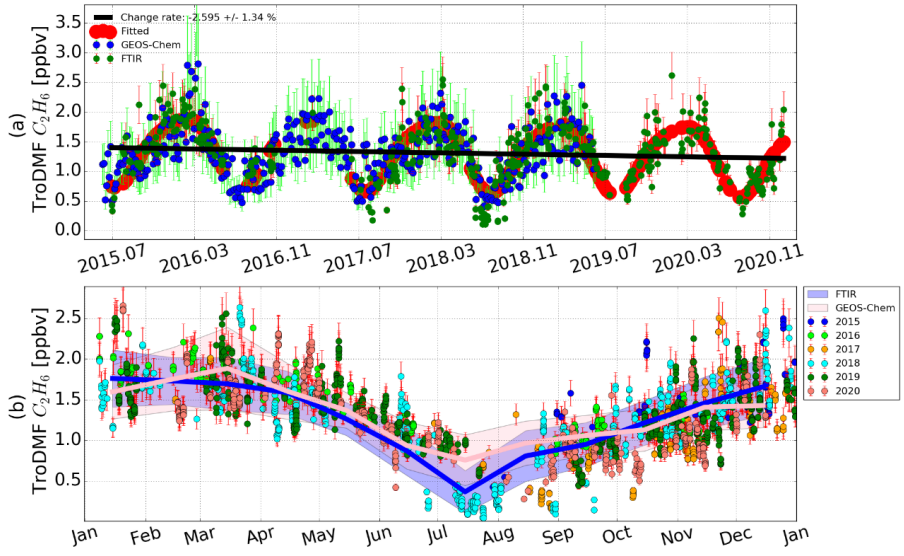

Fig. 3. (a) C_2H_6 troDMF time series comparison between FTIR observation and GEOS-Chem model BASE simulation from 2015 to 2020 over Hefei, eastern China. The seasonality and interannual variability are represented by red dots and black line, respectively, which are fitted by using a bootstrap resampling model with a 3rd Fourier series plus a linear function. (b) Seasonal variations of C_2H_6 troDMF by FTIR and GEOS-Chem simulation. Bold curves and the shadows are monthly mean values and the 1-σ standard variations, respectively. Vertical error bars for FTIR and GEOS-Chem represent retrieval uncertainties and diurnal variabilities, respectively.

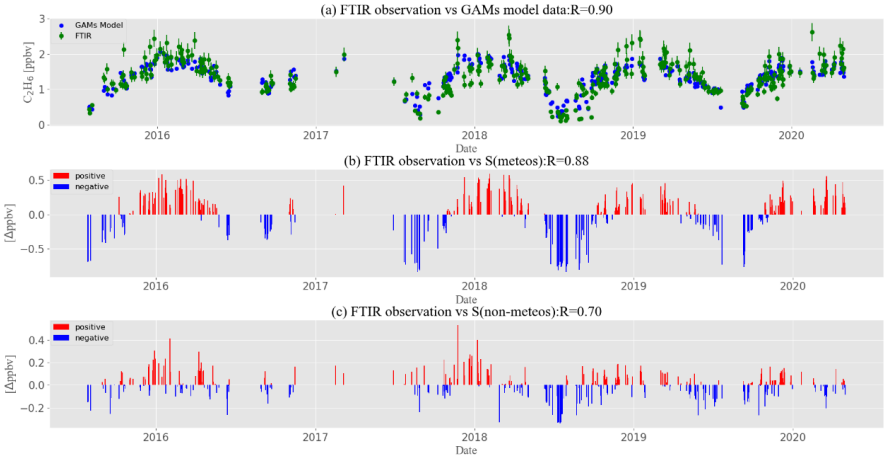

Fig. 4. (a) C_2H_6 troDMF time series from 2015 to 2020 over Hefei, eastern China by FTIR and GAMs regression model. (b) Time series of accumulated meteorological smooth functions (S(*meteos*)), and (c) time series of accumulated emission smooth functions (S(*non-meteos*)). Positive and negative influences are indicated with red and blue bars, respectively. Correlation coefficients for the total, meteorological, and emission influences are also shown.

https://doi.org/10.5194/acp-2021-13
Preprint. Discussion started: 22 March 2021

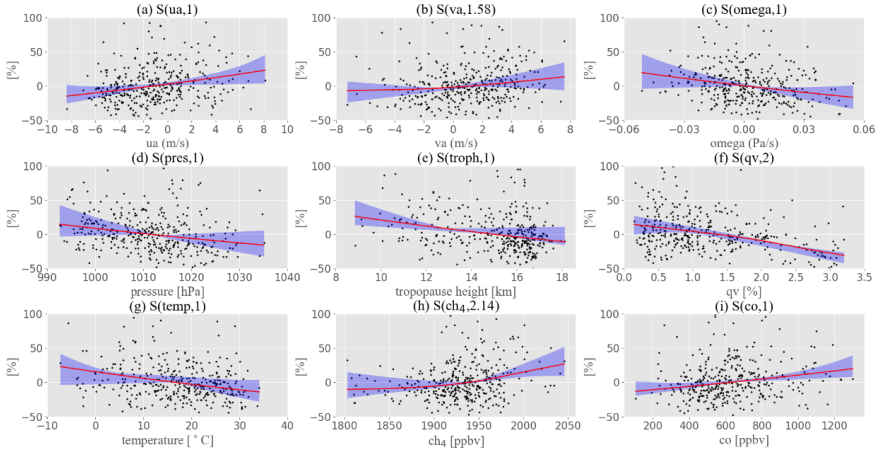

Fig. 5. Influence of each individual variable in the GAMs model on C_2H_6 troDMF from 2015 to 2020 over Hefei, eastern China. (*a*) to (*i*) are for zonal wind (*ua*), meridional wind (*va*), convection wind (*omega*), pressure (*pres*), tropopause height (*troph*), H_2O troDMF (*qv*), temperature (*temp*), CH_4 troDMF (*ch4*), and CO troDMF (*co*), respectively. The DOFS of each smoothing function is included in the bracket in each panel. The *x*-axis represents variation range of each variable and the *y*-axis represents relative percentage change of C_2H_6 troDMF relative to its annual mean value.

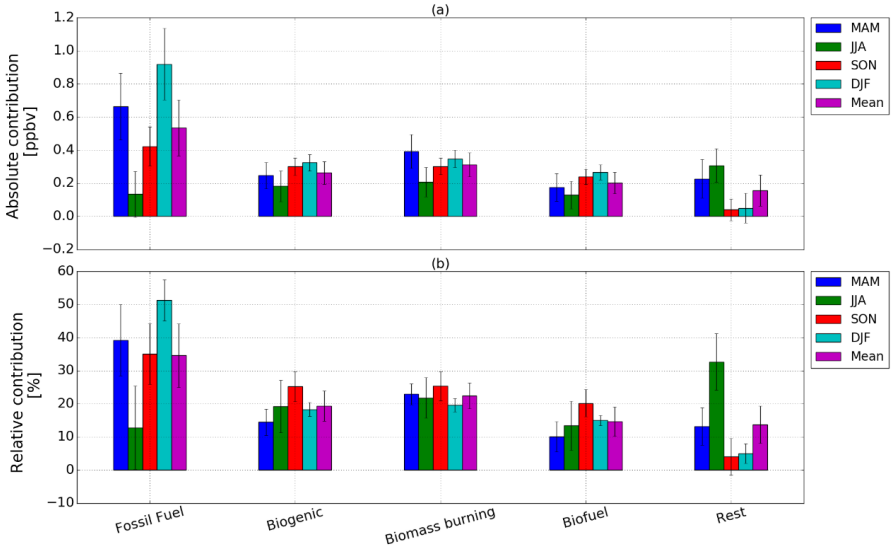

Fig. 6. Absolute (a) and relative (b) contributions of fossil fuel, biogenic, biomass burning, and biofuel emission sources to the observed C_2H_6 abundance from 2015 to 2020 over Hefei, eastern China. The remaining contribution calculated as the difference between the BASE simulation and the sum of anthropogenic and natural contributions is also shown. All contributions are grouped by season. Vertical error bars represent 1-σ standard variation.

https://doi.org/10.5194/acp-2021-13
Preprint. Discussion started: 22 March 2021

Atmospheric Chemistry and Physics Discussions

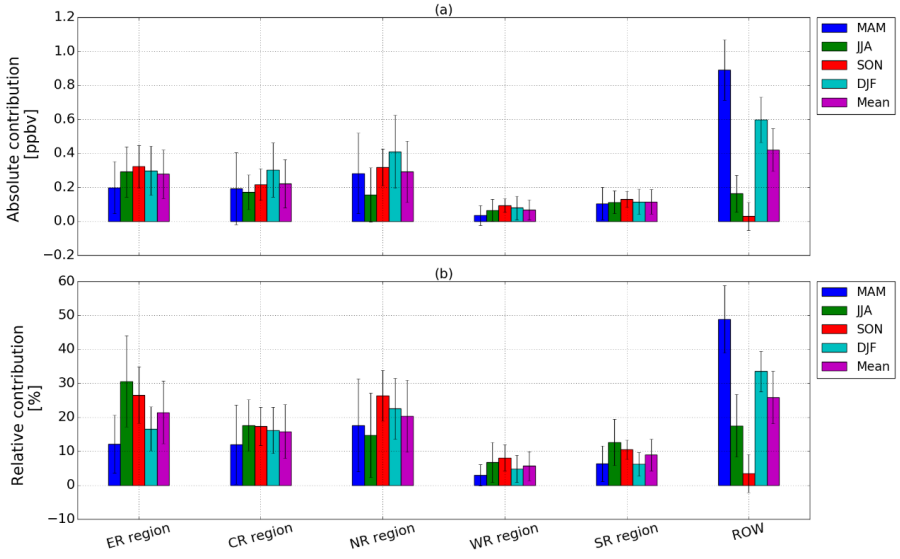

Fig. 7. Absolute (a) and relative (b) contributions of ER, CR, NR, WR, SR, and ROW regions to the observed C_2H_6 abundance from 2015 to 2020 over Hefei, eastern China. All contributions are grouped by season. Geographical definition of each region is summarised in Table 3. Vertical error bars represent 1-σ standard variation.

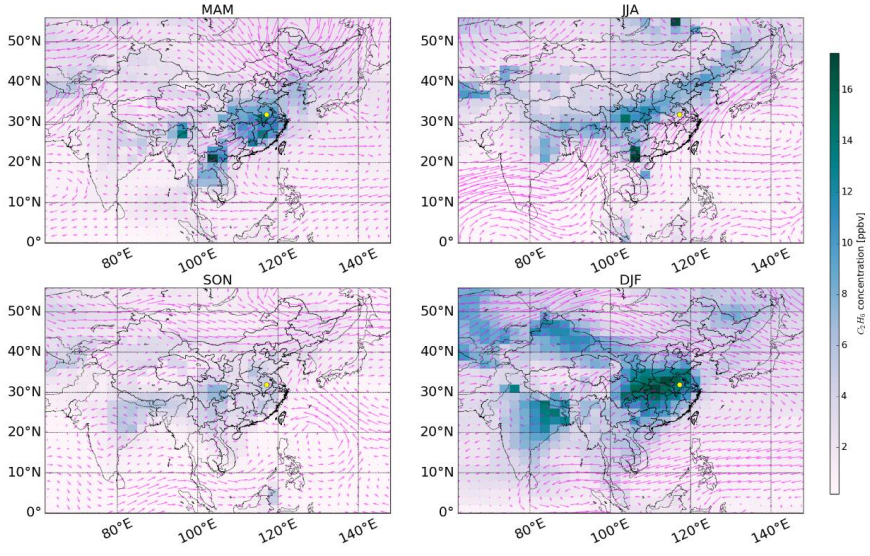

Fig. 8. Spatial distribution of C_2H_6 tropDMF in the GEOS-Chem BASE simulations in different seasons. The arrows indicate horizontal wind vectors at 900 hPa; the observation site is marked with a yellow dot. Meteorological fields are from the GEOS-FP 0.25° × 0.3125° dataset.

https://doi.org/10.5194/acp-2021-13
Preprint. Discussion started: 22 March 2021

Atmospheric Chemistry and Physics Discussions

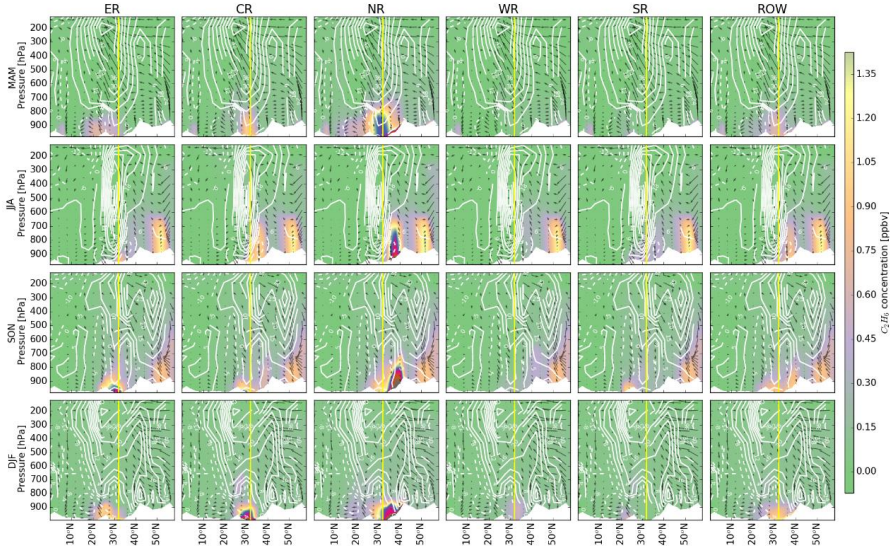

Fig. 9. The first row shows the latitude–height distributions of C_2H_6 VMR averaged over 113–121° E in spring (MAM), originating in different source regions (corresponding to different columns). See Table 3 for latitude and longitude definitions. The white area indicates topography, and the white contours at intervals of 6 m s^{-1} are the easterly (dashed) and westerly (solid) mean meridional winds; the wind vectors (consisting of zonal wind in m s^{-1} and vertical velocity in units of Pa s^{-1}) are represented by arrows; the observation site is marked with a yellow line. The second to fourth rows are the same as the first row but for summer (JJA), autumn (SON), and winter (DJF), respectively. Meteorological fields are from the GEOS-FP 0.25° × 0.3125° dataset.

Appendix.

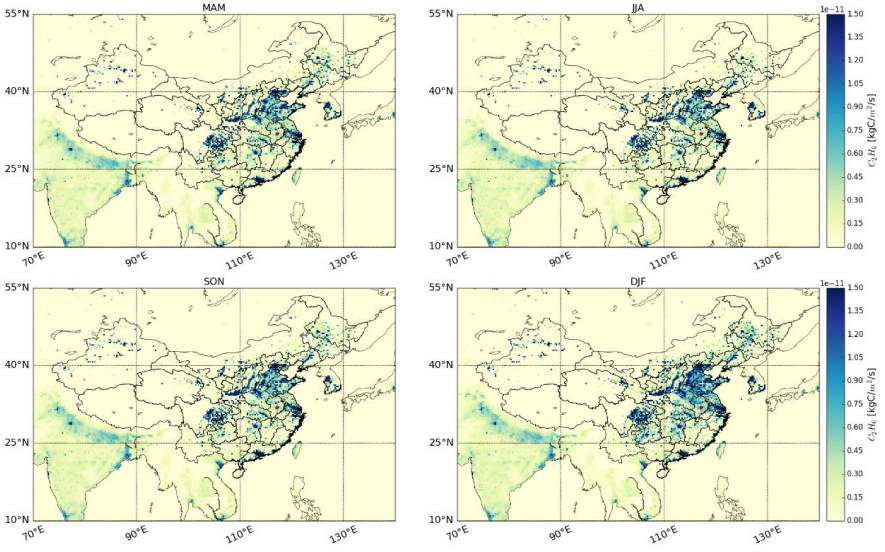

Fig. A1. C_2H_6 emission distribution in 2019 (0.25°×0.25°) from the Multi-resolution Emission Inventory for China (MEIC) over China and surroundings. Units are in kgC/m^2/s. The observation site is marked with a red dot.